CATALYST-FREE GALLIUM NITRIDE NANOWIRE NUCLEATION

By

Kaylee McElroy

A THESIS

Submitted to
Michigan State University
in partial fulfillment of the requirements
for the degree of

MASTER OF SCIENCE

Electrical Engineering

2009

ProQuest LLC
789 East Eisenhower Parkway
P.O. Box 1346
Ann Arbor, MI 48106-1346

ABSTRACT

CATALYST-FREE GALLIUM NITRIDE NANOWIRE NUCLEATION

By

Kaylee McElroy

Extensive research on nanowire devices and applications has unleashed exciting possibilities in a quest for smaller, faster electronic equipment, more sensitive detectors, and new devices that take advantage of the quantum mechanical world. One of the roadblocks to these new technologies is a clear understanding of how nanowires are formed and how to control their growth. Nanowire growths can be grouped in two broad categories: catalytic growths and catalyst-free growths. Catalyst-free nanowire growths are useful in applications where catalyst particles are not desirable.

This thesis deals exclusively with gallium nitride catalyst-free nanowire nucleation and growth mechanisms. GaN nanowires are of particular interest because of GaN's unique optical and electronic properties. This thesis contributes fundamental understanding of the formation mechanisms of catalyst-free GaN nanowire growth through investigations of the matrix from which the nanowires grow and through novel use of the nanowires themselves as a diagnostic of their own growth mechanism. This work shows that nanowire orientation changes as a function of growth temperature and investigates this orientation change in terms of availability of nucleation sites and constituent adatom materials.

TABLE OF CONTENTS

LIST OF TABLES

LIST OF FIGURES

Chapter 1

Introduction

Gallium nitride (GaN) nanowires have been under extensive investigation in recent years due to their unique optical and electrical properties. GaN nanomaterials are currently extensively researched due to interest in their potential for applications such as blue nanowire lasers [12] and high electron mobility transistors (HEMTs) [13]. For device applications, control of crystalline quality and orientation is essential. The nanowire nucleation and growth mechanisms are not well understood, and it is critical to understand these mechanisms in order to develop controlled nanowire growth processes.

The nanowires used in this study were grown using a catalyst-free growth method. Catalyst free nanowire growths have no metal impurities in the nanowires and can be used in applications where device fabrication steps are incompatible with the presence of a metal catalyst [14, 15]. Investigations using multiple analysis techniques have been performed by our group and have contributed new understanding of nanowire structures. First, we have demonstrated that the nanowire growth orientation is influenced by growth temperature in catalyst free growth. Original work presented in this thesis will discuss the dynamic evolution of the growth matrix that controls the availability of nucleation sites and how the matrix effects nanowire orientation. This

thesis further explores the nucleation mechanisms that result in the observed nanowire orientations and discusses the availability of constituent adatom materials. Second, we have demonstrated that GaN nanowires from the growths studied have internal crystal structures that continue along the entire length of the nanowire. Within this thesis the internal nanowire structure is used as a diagnostic for the nanowire growth mechanism. Understanding how and why internal nanowire structures form is critical for successful nanowire device engineering.

The remainder of chapter one deals with the basic physics and crystallography necessary to understand GaN devices. Chapter two discusses factors that are known to affect catalytic and non-catalytic nanowire growths. Additionally, an outline of crystal growth theories is provided. Chapter three covers the various instruments used to characterize the samples and explains how they operate and what information relevant to the present investigations can be obtained from using them. The main experimental results are presented in chapter four. Models for growth mechanisms based on the experimental results are presented in chapter five. The final chapter summarizes the main achievements of this thesis and discusses future research directions.

1.1 The Band Structure of Semiconductors

Each electron of a single atom is only allowed to have certain energies, or in other words, the energy of the electrons is *quantized*. When two atoms bond together, their energy levels split into bonding and anti-bonding molecular orbitals. The molecular orbital structure for GaN is shown in Figure 1.1. The molecule can exist as long as more bonding orbitals are filled with electrons when compared with filled anti-bonding orbitals.

As more and more atoms are added to the molecule, the energy levels continue to

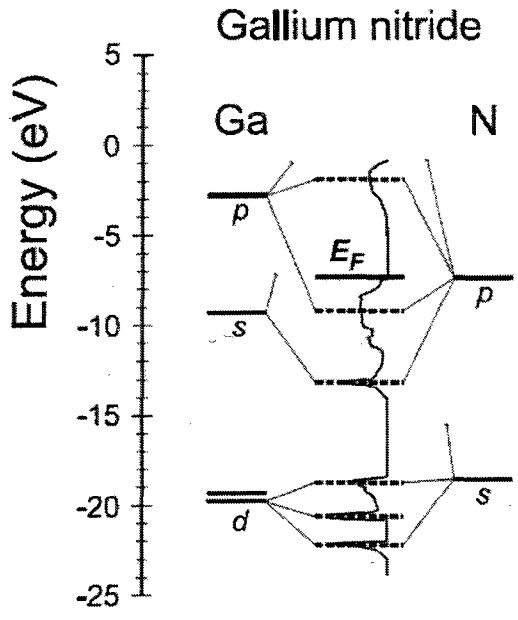

Figure 1.1: Free atom electron energy levels for Ga and N are shown on either side. Molecular orbitals of GaN are displayed in between. (This image is from Dudesek *et al.* [1].)

split as the electron orbitals interact. Adding a large number of atoms, resulting in a three dimensional solid, causes the energy levels to be so close together that energy can be thought of as having bands of continuous values, instead of discreet values.

However, even if there are an infinite number of atoms in a solid, there may still be electron energy levels that are not allowed. This gives rise to the *band structure* of the solid. The groups of energies that are allowed are known as *energy bands*, and the groups of energies that are not allowed are known as *band gaps*. The highest energy band that has electrons in it at 0K is known as the *valence band*, and the next highest energy band is known as the *conduction band*. Electrons in the valence band are in bonds and are therefore not free to move about the solid like electrons in the conduction band are. The band structure of a solid has an enormous impact on the electrical properties of the solid. If the highest energy electrons are at the very top

of an energy band and there is a large band gap above the band, the material is an insulator because the electrons are unlikely to acquire enough energy to go to the next energy level. Because an insulator has no electrons in the conduction band, the solid will not conduct electricity very well. If the valence band and the conduction band overlap, the material is a metal because electrons can easily gain enough energy to get to the next level and move throughout the solid. A third case occurs when there is a relatively small band gap above the valence band; these materials are known as semiconductors. Electrons in a semiconductor can gain sufficient energy to get to the conduction band by absorbing the energy of either a photon or a phonon (a phonon is a quantized lattice vibration due to thermal energy). There is no set band gap width that determines whether a material is an insulator or a semiconductor so the distinction is usually made in the way the material is used.

The band structure of a solid also depends on the structure of the crystal. The energy $\hat{E}$ of an electron is dependent on the wave vector $\hat{k}$ since

$$\begin{aligned} \hat{E} &= \frac{\hat{p}^2}{2m^*} \\ \hat{p} &= \hbar\hat{k} \end{aligned} \tag{1.1}$$

where $\hat{p}$ is the momentum and m^* is the effective mass of the electron. Thus $\hat{E}$ is dependent on the individual electron's momentum as it travels through the crystal lattice. The band structures of zinc-blende and wurtzite GaN as a function of the wave vector is plotted in Figure 1.2.

The *energy density of states* $g(E)$, which is the number of allowed states at each energy level in an energy band, is dependent on the dimensionality of the crystal. For a three dimensional crystal, $g_{3D}(E) \propto \sqrt{E}$, so the number of allowed states smoothly increases at higher energy levels (see Figure 1.3). When momentum is restricted in one dimension (i.e. the crystal is shaped like a two dimensional flat plane only a

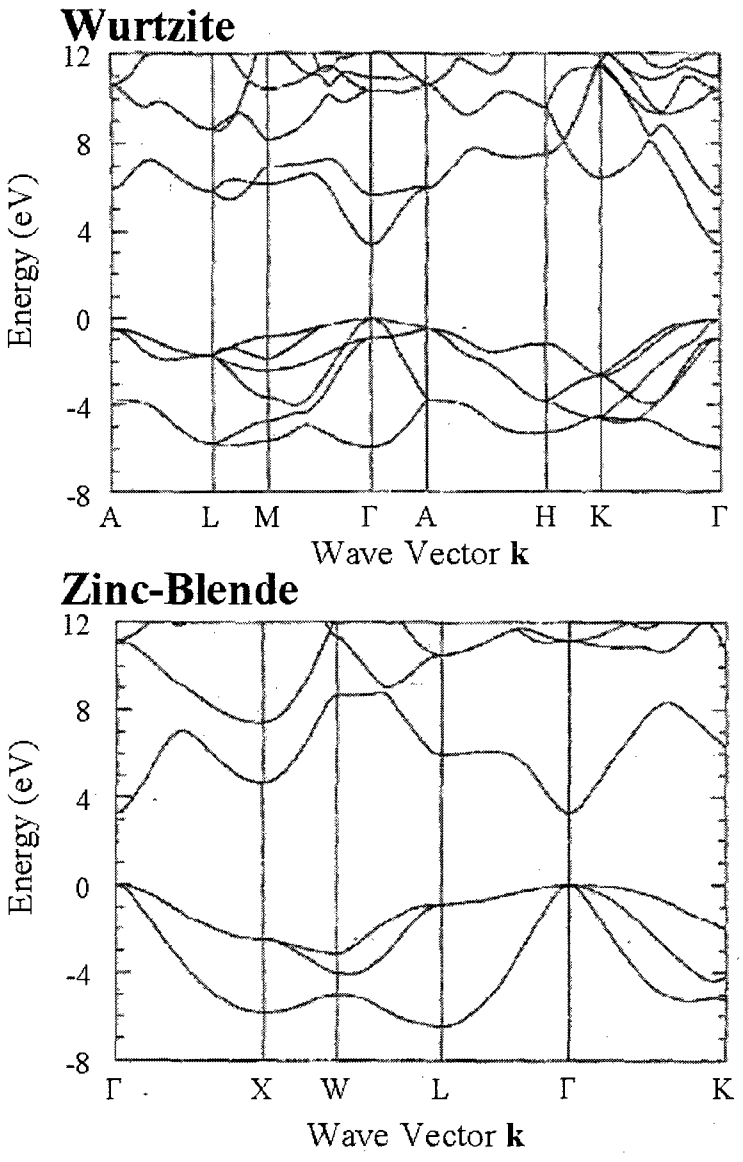

Figure 1.2: Calculated pseudopotential band structures for wurtzite (top) and zinc-blende (bottom) GaN. Symmetry points of the Brillouin zone for the appropriate crystal lattice are marked along the x-axis. (This image is from Kolnik *et al.* [2].)

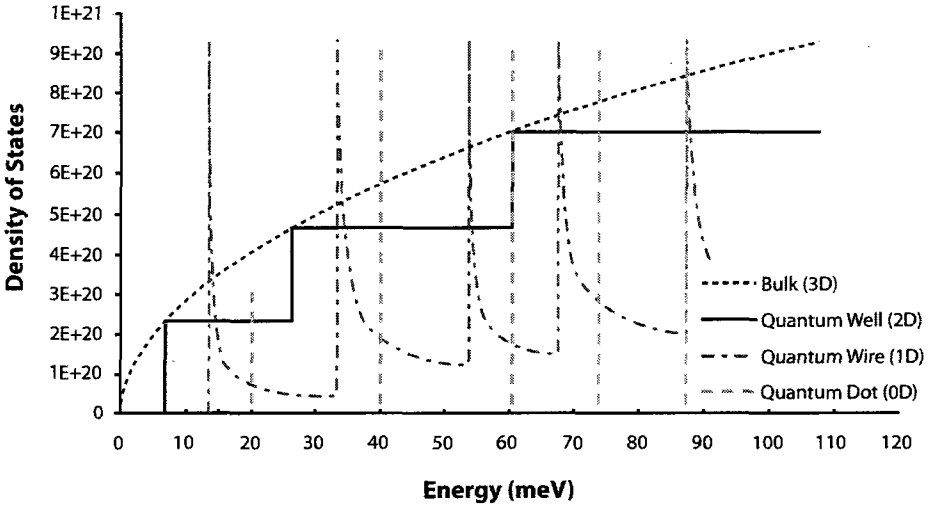

Figure 1.3: Density of States of zero, one, two, and three dimensions. (This figure is subject to the GNU Free Documentation License Version 1.2 or any later version published by the Free Software Foundation.)

few nanometers thick) the energy states in the corresponding direction are quantized. The energy states in this thin crystal plane may be approximated by a 1D quantum well. In this case, $g_{2D}(E) \propto C_n$ where C_n is a constant corresponding to the n^{th} energy level of the quantum well. C_n increases with higher energy. When a crystal is restricted in two dimensions so that it is shaped like a wire, $g_{1D}(E) \propto \frac{D_n}{\sqrt{E}}$ where D_n is a constant corresponding to the n^{th} energy level of the quantum wells. This means that there are relatively large numbers of available energy states near the energy levels of the quantum wells. The conductivity (which is related to the density of states) of a theoretical wurtzite GaN nanowire is shown in Figure 1.4. If all three dimensions are restricted, a quantum dot is formed. The quantum dot acts much like an atom because only specific energy levels are allowed for the electrons; all other energy levels are forbidden.

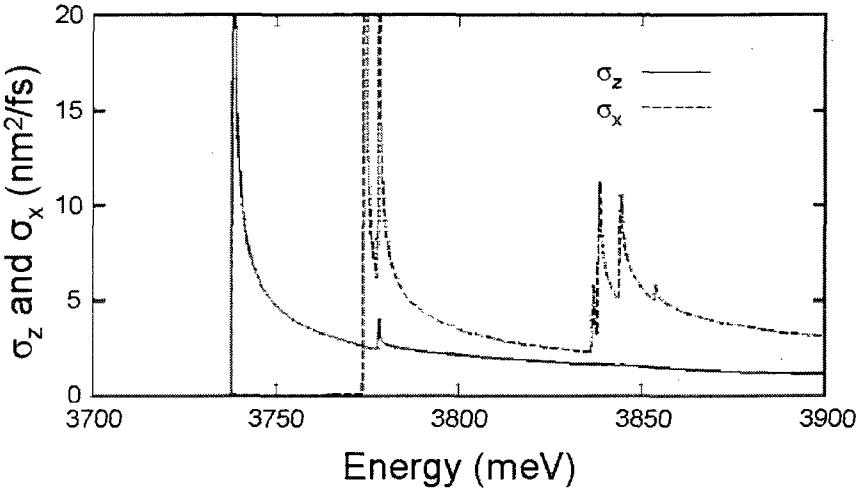

Figure 1.4: Theoretical calculation of the conductivity along the axis σ_z and perpendicular to the axis σ_x for a cylindrical wurtzite GaN wire with a radius of 2.5 nm. The 1D density of states influences the conductivity of the nanowire. (This figure is from Maslov and Ning [3].)

1.2 Present and Future Applications of Gallium Nitride

1.2.1 Photonic Applications

There is no set band gap width that determines whether a material is an insulator or a semiconductor; the distinction is usually made in the way the material is used. Gallium nitride is what is known as a *wide band gap* semiconductor because it has a larger band gap than most traditional semiconductors. This wide band gap is one reason why GaN is a good material to produce blue-violet light. In bulk material, wurtzite GaN has a bandgap of 3.39 eV, resulting in an emitted wavelength of approximately 366 nm ($\lambda = \frac{hc}{E_W}$) [16]. Likewise, the bandgap of bulk zinc-blende GaN is 3.2 eV, resulting in an emitted wavelength of approximately 387 nm. Gallium nitride is also a *direct band gap* semiconductor. The electron energy levels are different for the

various orientations within the crystal structure. When the minimum energy level of the conduction band occurs at the same crystal orientation as the maximum energy level of the valence band (as in Figure 1.2), the material is known as a direct band gap semiconductor. In a direct band gap material, if an electron in the conduction band loses energy and goes to the valence band, the lost energy is emitted in the form of a photon with energy approximately equal to that of the band gap. Until the 1990's, blue LEDs were made out of SiC, which is an indirect bandgap material, and therefore the devices had very low efficiencies. In 1993 Shuji Nakamura created the first high-brightness blue LEDs using an InGaN/AlGaN double heterostructure [17]. This breakthrough has been critical to the development of full color LED displays and white LEDs. Since then efficiencies of GaN based LEDs have increased even more as device design and fabrication techniques are refined [18]. Additionally, the availability of GaN substrates with low dislocation densities has added to the efficiency and lifetime of blue LEDs and laser diodes [19].

Current research is introducing the use of 1D GaN nanowires for photonic applications. UV lasers have been created from GaN quantum wires [12, 20]. Additionally, GaN nanowires have been used to create ultra violet LEDs by positioning an n-type GaN nanowire so that it crosses a p-type Si nanowire [21].

1.2.2 Electronic Applications

A high electron mobility transistor (HEMT) uses two materials with different bandgaps to create a quantum well to trap the electrons in a high quality crystal. HEMTs are capable of handling large amounts of current because the quantum well region does not have any dopants in it (dopants can scatter or trap the electrons and impede the electron mobility). AlGaN/GaN HEMTs have been fabricated [22, 23], and have potential to be used for high power, high frequency applications because GaN is able to withstand high voltages [24, 23, 13] and has higher efficiencies than the current

standard silicon technology [13]. The lowest energy in the conduction band of AlGaN is higher than the lowest energy in the conduction band of GaN, thus electrons will get trapped in the GaN layer. Controlling the polarity of the GaN is important for HEMTs [25].

GaN nanowire field effect transistors (nanoFETs) made from individual GaN nanowires have been fabricated [26, 27]. GaN nanoFETs have been electrically tested to show that the electron mobility of the devices can be between 150-650 $cm^2/V{\cdot}s$ which is comparable to or better than 100-300 $cm^2/V{\cdot}s$ for thin film GaN [26]. A nanoFET fabricated using a multiphase nanowire showed high current density consistent with results reported from single phase nanowire systems [27].

1.3 Crystal Structures of GaN

For maximum performance of photonic and electronic applications, the crystal structure of GaN nanowires should be defect free. Therefore, it is important to understand the crystalline nature of GaN. GaN can form in either the zinc-blende or the wurtzite crystal structures. The zinc-blende structure is closely related to the face centered cubic (fcc) structure, and the wurtzite structure is closely related to the hexagonal close pack (hcp) structure. In turn, fcc and hcp are very similar structures. This section will explain the details of the zinc-blende and wurtzite structures and how they are related. It will also cover the basics of hexagonal crystal notation, which is often left out of introductory solid state textbooks.

The conventional unit cell of an fcc structure has a Type I atom at each corner of the cube and in the center of each face of the cube (see Figure 1.5a). The zinc-blende structure is formed by adding a Type II atom $\frac{a}{4}(\hat{x}, \hat{y}, \hat{z})$ away from each Type I atom where a is the length of a side of the cube, as shown in Figure 1.5b.

An hcp structure has Type I atoms at each corner of a hexagonal prism, in the

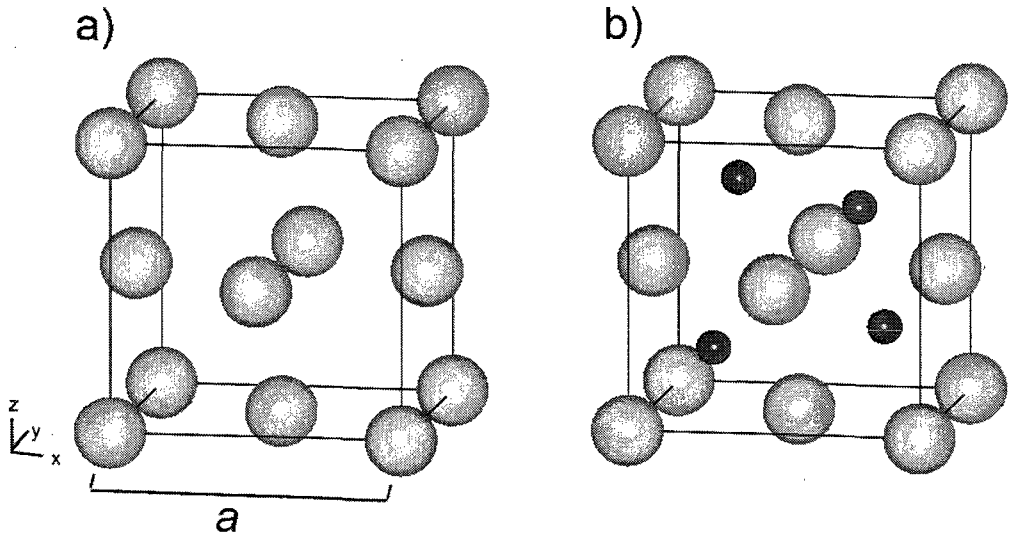

Figure 1.5: a) the fcc crystal structure. b) the zinc blende structure has a different species of atom located at $(\frac{1}{4}\hat{x}, \frac{1}{4}\hat{y}, \frac{1}{4}\hat{z})$. In both a) and b) the lines mark the boundaries of the conventional unit cell. (Images produced using the VESTA software package [4])

center of each hexagonal face, and three atoms which are half-way in between the hexagonal faces and nestled in the cavities formed by the atoms in the hexagonal faces (see Figure 1.6a). The wurtzite structure is formed by adding a Type II atom directly above each Type I atom in the c direction, as shown in Figure 1.6b. While it can be easier to picture these crystal structures with a full hexagonal base, the conventional unit cell consists of $\frac{1}{3}$ of the hexagon base, as shown in Figure 1.7.

The fcc and hcp structures are closely related. In order to see this, it is necessary to realize that the (111) plane of the fcc structure is equivalent to the (0001) plane of the hcp structure. If we start with the (111)/(0001) plane and start adding the next layer of atoms, the atoms will position themselves in the wells in between the base layer of atoms for both fcc and hcp, as shown in Figure 1.8. With the third layer of atoms, however, the structures differ. In the hcp structure, the third layer of atoms forms directly above the first layer. The third layer of atoms in the fcc structure stack

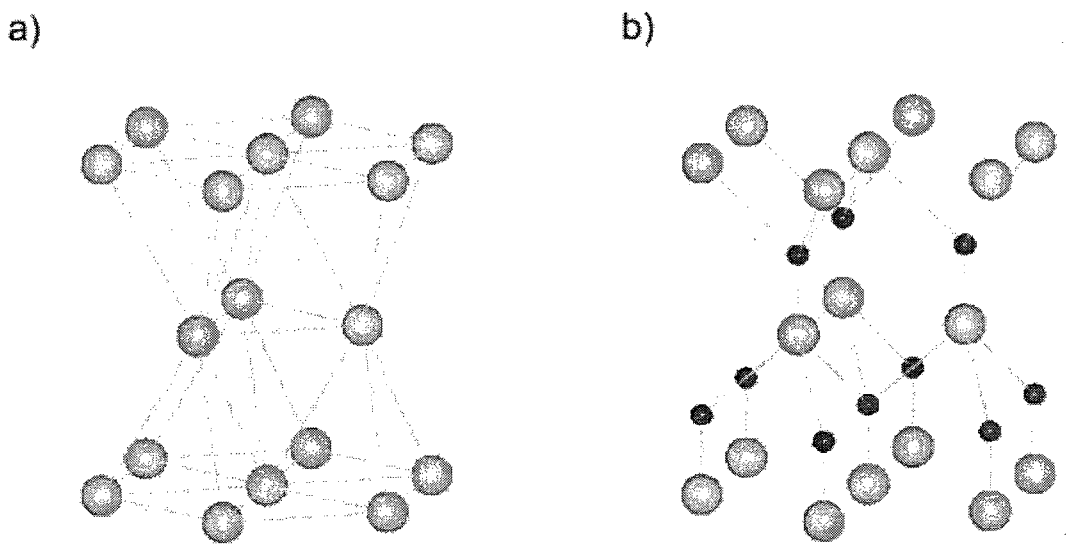

Figure 1.6: a) the hcp crystal structure. b) the wurtzite structure has one Type II atom directly above each Type I atom of the hcp structure. In both a) and b) the lines indicate nearest neighbors. Lines are drawn between nearest neighbors, and the number of lines touching each atom in the crystal structure is the *coordination number* of the crystal structure. (Images produced using the VESTA software package [4])

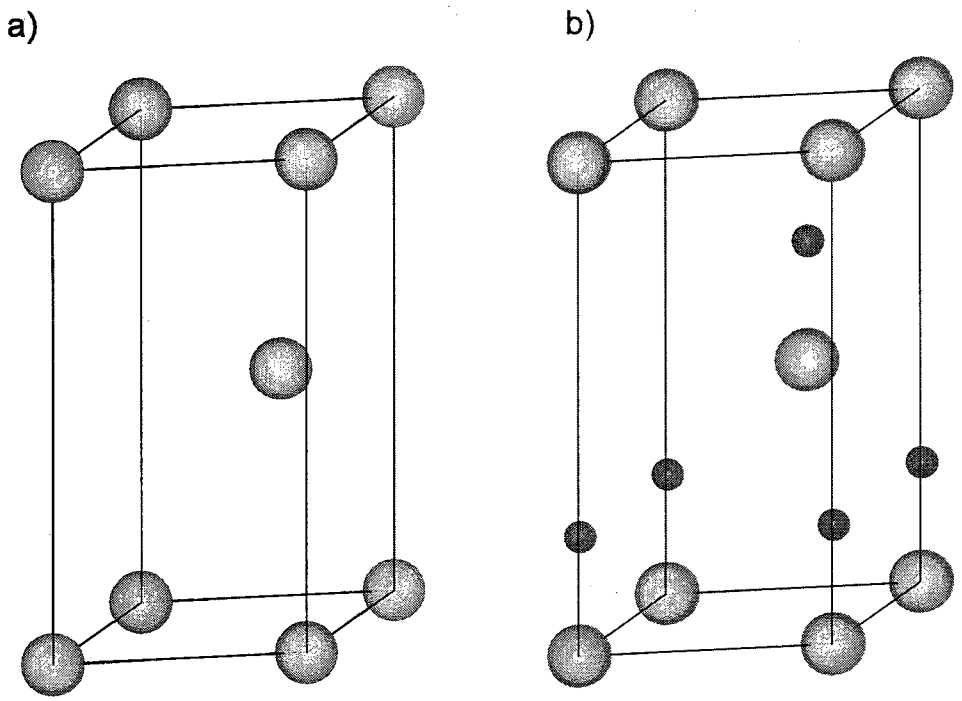

Figure 1.7: a) the hcp unit cell. b) the wurtzite unit cell. In both a) and b) the lines mark the boundaries of the conventional unit cell. (Images produced using the VESTA software package [4])

in the cavities that are not directly above the first layer. This difference gives rise to the notation that hcp has ABAB stacking and fcc has ABCABC stacking.

Another thing to note is that GaN, like many other crystals, has both a covalent and an ionic character in its bonding. The ionic character of the bond can be quantitatively defined by the Phillips ionicity, f_i, of the crystal. f_i is zero for a perfectly covalent bond, and one for a perfectly ionic bond, so it can be thought of as the percent of ionicity of the bond [28]. For zinc-blende, $f_i = 0.519$, and for wurtzite $f_i = 0.500$ [29, 30]. The ionic nature of the bond causes planes that have uneven numbers of gallium and nitrogen atoms to be polar. For example the (0001) wurtzite plane is polar because it contains atoms of only one species.

Crystal planes and directions are conveniently described using the Miller indices (hkl). Because crystals are three dimensional materials, only three vectors are required to describe the crystal planes. Cubic structures, such as zinc-blende, are easily described using the vectors $\hat{x}$, $\hat{y}$, and $\hat{z}$. Hexagonal crystals, on the other hand, are typically described using four vectors, three pointing out of every other corner of a flat hexagon ($\hat{a}_1$, $\hat{a}_2$, and $\hat{a}_3$) and one perpendicular to the plane of the hexagon ($\hat{c}$) (see Figure 1.9a). Four digit Miller-Bravais indices $(hkil)$ use all four directions, and the i index corresponds to the $\hat{a}_3$ direction. However, the $\hat{a}_3$ direction is redundant because

$$\hat{a}_3 = -(\hat{a}_1 + \hat{a}_2) \tag{1.2}$$

Or equivalently,

$$\hat{a}_1 + \hat{a}_2 + \hat{a}_3 = 0 \tag{1.3}$$

For hexagonal systems, three digit Miller indices (hkl) are derived from the $\hat{a}_1$, $\hat{a}_2$, and $\hat{c}$ directions, respectively. To switch $(hkil)$ to Miller notation, simply remove the i index (i.e. $(10\bar{1}0) = (100)$). To switch (hkl) to Miller-Bravais notation, get the i term by adding the h and k terms and multiplying that sum by -1 (i.e. $(111) = (11\bar{2}1)$ since

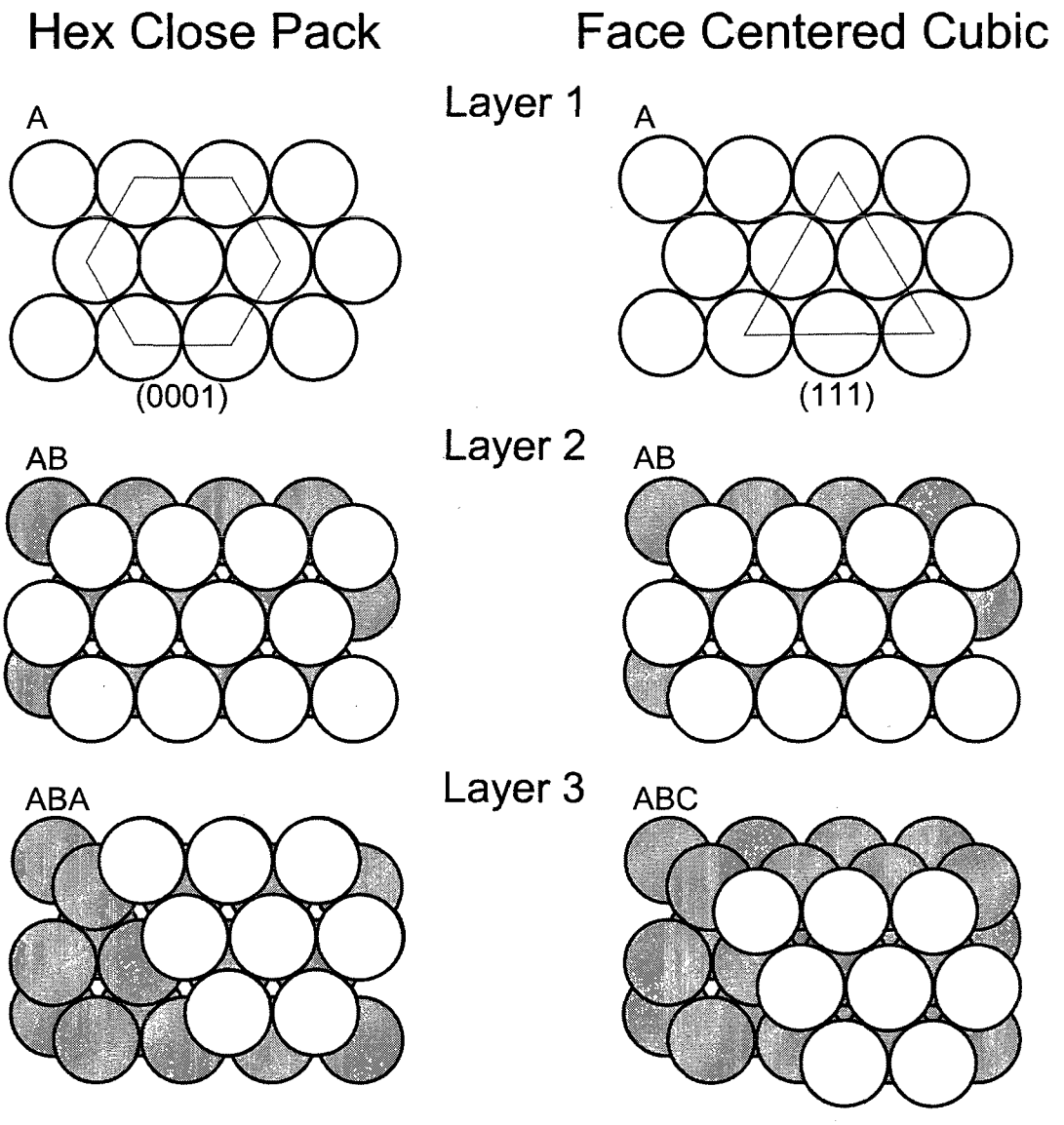

Figure 1.8: Layer 1: The (0001) and (111) planes are identical. Layer 2: Atoms stack in the cavities between the atoms of the first layer. Layer 3: The third layer of hcp stacks directly above the first layer. The third layer of fcc stacks in the cavities that are not directly above the first layer.

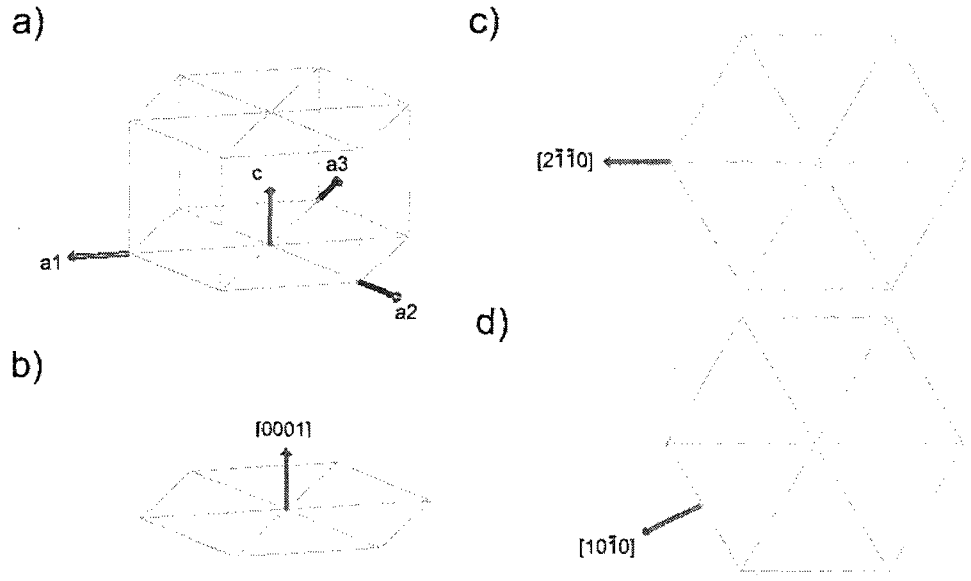

Figure 1.9: Miller-Bravais notation in the hexagonal system. a) The lattice vectors are $\hat{a}_1$, $\hat{a}_2$, $\hat{a}_3$, and $\hat{c}$. b), c), and d): Directions perpendicular to the c, a, and m faces, respectively. (Image produced using the VESTA software package [4])

$-(1+1) = -2$). The advantage of the four digit notation for hexagonal symmetries is that it makes equivalent planes easier to see. For example,

$$\begin{aligned} \{11\bar{2}0\} &= (11\bar{2}0), (\bar{2}110), (1\bar{2}10) \\ &= (110), (\bar{2}10), (1\bar{2}0) \end{aligned} \tag{1.4}$$

In the three digit notation, it is not obvious that (110) is related to ($\bar{2}$10) and (1$\bar{2}$0), but including the fourth digit shows the symmetry of the related directions. However, the three digit notation is used in all computations (because i is redundant), and all other crystal structures use the same three digit notation.

The Miller index for a direction is given by the smallest integers whose ratio $u : v : w$ is equivalent to the ratio of lengths along the $\hat{a}, \hat{b}$, and $\hat{c}$ directions of the vector $\hat{R}$ pointing in the given direction. Only for cubic systems is the direction $[hkl]$

perpendicular to the (hkl) plane. Generally, the direction perpendicular to the (hkl) is $[uvw]$, and $[uvw] \neq [hkl]$.

In hexagonal systems, vector directions can be expressed as three or four digit indices. For three digit indices, $\hat{R} = u\hat{a}_1 + v\hat{a}_2 + w\hat{c}$, and $[uvw]$ is the three digit Miller index for the direction. For four digit direction indices, $\hat{R} = U\hat{a}_1 + V\hat{a}_2 + T\hat{a}_3 + W\hat{c}$ where $T = -(U+V)$. The four digit Miller-Bravais index for the direction is $[UVTW]$.

Given a random direction, the direction vector may be expressed as

$$\hat{R}_1 = U\hat{a}_1 + V\hat{a}_2 + T\hat{a}_3 + W\hat{c} \tag{1.5}$$

or

$$\hat{R}_2 = u\hat{a}_1 + v\hat{a}_2 + w\hat{c} \tag{1.6}$$

where $\hat{R}_1$ and $\hat{R}_2$ point in the same direction but may not have the same magnitude. In other words, $\hat{R}_1 = n\hat{R}_2$. Since $\hat{a}_3 = -\hat{a}_1 - \hat{a}_2$,

$$\begin{aligned} \hat{R}_1 &= U\hat{a}_1 + V\hat{a}_2 - T\hat{a}_1 - T\hat{a}_2 + W\hat{c} \\ &= (U-T)\hat{a}_1 + (V-T)\hat{a}_2 + W\hat{c} \end{aligned} \tag{1.7}$$

so

$$\begin{aligned} u &= \frac{U-T}{n} \\ v &= \frac{V-T}{n} \\ w &= \frac{W}{n} \end{aligned} \tag{1.8}$$

This system of equations can be solved for U, V, T, and W in terms of u, v, and w in order to switch from the three digit notation to the four digit notation. n is chosen to get the lowest valued integers which point in the direction of $\hat{R}$. As an example,

consider the direction $[\bar{2}110]$ which points out one of the corners of the hexagon in the c-plane and gives $\hat{R}_1$ a magnitude of 3. Converting to the three digit notation,

$$\begin{aligned} u &= \frac{^{-}2-1}{n} \\ v &= \frac{1-1}{n} \\ w &= \frac{0}{n} \end{aligned} \tag{1.9}$$

gives $\left[\frac{-3}{n}00\right]$. n is chosen to be 3 for this example so that $\hat{R}_2$ has the smallest magnitude in the desired direction. Thus $[\bar{2}110] = [100]$. Once again, the three digit notation is used in computations and computer software because all other crystal structures use the same notation.

The interplanar spacing for hexagonal crystals is given by [31]

$$\frac{1}{d^2} = \frac{4}{3}\frac{h^2+hk+k^2}{a^2} + \frac{l^2}{c^2} \tag{1.10}$$

The angles between planes for hexagonal crystals is given by [31]

$$\cos\phi = \frac{h_1h_2 + k_1k_2 + \frac{1}{2}(h_1k_2+h_2k_1) + \frac{3a^2}{4c^2}l_1l_2}{\sqrt{\left(h_1^2+k_1^2+h_1k_1+\frac{3a^2}{4c^2}l_1^2\right)\left(h_2^2+k_2^2+h_2k_2+\frac{3a^2}{4c^2}l_2^2\right)}} \tag{1.11}$$

and angles between directions for hexagonal crystals is given by [32]

$$\cos\rho = \frac{u_1u_2 + v_1v_2 - \frac{1}{2}(u_1v_2+v_1u_2) + \frac{c^2}{a^2}w_1w_2}{\sqrt{\left(u_1^2+v_1^2-u_1v_1+\frac{c^2}{a^2}w_1^2\right)\left(u_2^2+v_2^2-u_2v_2+\frac{c^2}{a^2}w_2^2\right)}} \tag{1.12}$$

Chapter 2

Nanowire Growth and Nucleation

The exact growth mechanisms of nanowires are still being debated. Nanowires can be formed by two general growth methods: catalytic and non-catalytic. While catalytic growths have been studied extensively in recent years, non-catalytic growths may be able to provide a greater variety of nanostructures for specific applications if the growth can be controlled. Additionally, non-catalytic growths have no metal impurities in the nanowires and can be used in applications where device fabrication steps are incompatible with the presence of a metal catalyst [14, 15]. This chapter reviews literature for both catalytic and non-catalytic nanowire growth. Additionally, relevant crystal formation theories are discussed.

2.1 Catalytic Growth

A typical catalytic nanowire growth uses a substrate coated with nanoscale metal beads (often Au or Ni) to act as a catalyst for the nanowires. The vapor liquid solid (VLS) growth mechanism can be described by three stages: alloying, nucleation, and axial growth [33]. When the substrate is heated and gases containing the necessary elements for the nanowires flow over the substrate, some of the gases get incorporated

into the metal beads. The catalyst particle attracts the reactants within a certain distance and thus acts as a sink in the chemical potential [34]. The incorporation of other elements into the metal catalyst is known as alloying. This incorporation *can* cause the beads to melt [33]. Once the catalyst is super-saturated with atoms absorbed from the vapor, atoms precipitate from the alloy, causing the nucleation of the wire. A nanowire is formed as atoms continue to precipitate, causing extension along the nanowire axis. Research indicates that the diameter of the nanowires is proportional to the size of the metal beads [35]. Additionally, patterning the metal catalyst can pattern the location of the as-grown nanowires [35]. If nanowires are grown on a substrate that matches their lattice, the growth can be epitaxial [35]. Nanowires often have preferred growth directions, although this can be influenced by the choice of substrate and the growth conditions such as annealing the catalyst before growth [34, 35]. GaN nanowires grown by VLS methods have resulted in nanowires that grow in the $\langle 0001 \rangle$ [36], $\langle 11\bar{2}0 \rangle$ [36, 37], $\langle 21\bar{3}0 \rangle$ [37], and $\langle 10\bar{1}0 \rangle$ [38] directions. Coaxial wires can be grown by first growing a nanowire and then changing the growth conditions to allow for lateral growth [34].

Not all growths that use metal catalysts fit the VLS model for growth. A study by Dick *et al.* has shown that gold particles used in growing InAs may only serve as a low energy interface for the reactants [39]. Group V elements do not accumulate in the metal beads, but the group III elements do [39, 40, 41]. GaN nanowires only lengthen when in a N rich environment; if the environment switches to be Ga rich, the wires will thicken [40].

2.2 Non-catalytic Growth

Non-catalytic growth is sometimes called vapor solid (VS) growth and the nanowire nucleation mechanisms differ from that of a catalytic growth. Less is known about

VS nanowire growth than VLS and other catalytic nanowire growths. Although little is known about the exact mechanisms of formation for the VS system, several parameters are known to change the nanowire and/or matrix crystal formation. VS growth mechanisms allow different structures to form because the system is not constrained by the catalyst. For example, using catalyst methods GaN preferentially grows in the $\langle 10\bar{1}0 \rangle$ direction [42]. GaN can grow in different directions using VS methods. Peng *et al.* grew nanowires in the $\langle 10\bar{1}1 \rangle$ direction or the $\langle 0002 \rangle$ direction, depending on the growth temperature [42]. Other factors that are known to influence the growth include: gas flow rate [43], temperature [44], and gas phase supersaturation [44, 45]. Thus, VS nanowire growth is sensitive to gas phase kinetics during the growth. Growth rates of nanowires have been calculated theoretically, and non-linear growth rates have been observed [46]. Additionally, the morphology of the crystals obtained from a VS growth is inherently dependent on the properties of the crystalline structure that is grown. The 0001 and $01\bar{1}1$ planes of wurtzite structures are polar due to the fact that only one species of atom is on the surface. This polarization affects the growth of GaN and other wurtzite crystals [43, 47, 48].

2.3 Crystal Growth Mechanisms

The surface of a solid inherently has a higher energy than the interior of a solid. This is because the atoms on the surface are not as satisfied with their bonds as the atoms in the bulk of the material. One way the surface energy can be lowered is to have low index facets on the crystal formations. Other ways a solid can lower the surface energy is through relaxation or surface reconstruction. Relaxation is where the layer of atoms at the surface have a shorter bond-length than normal with the layer of atoms underneath of them. In some solids, relaxation occurs by the top layer shifting laterally relative to the expected position, so that the atoms are in the wells

between the lower layer of atoms. Surface reconstruction refers to the surface having an entirely different crystalline structure than that of the bulk material, whereas for surface relaxation the structure is the same, just shifted a little.

In order for crystal growth to occur, more atoms must attach to the crystal surface than are removed. For this non-equilibrium condition to occur, the liquid or vapor from which new atoms are added to the surface must be supersaturated. The level of supersaturation will effect crystal growth.

Consider a single atom landing on an atomically flat surface. Such an atom is called an *adatom*. This single atom will be weakly bound to the place where it lands. Depending on the thermal conditions, the atom may jump back off of the surface or it may diffuse across the surface, jumping into nearby lattice positions [49]. The greater the number of bonds formed with an adatom, the lower the surface energy. So if there is another adatom in a lattice position adjacent to the first adatom, both atoms will be less likely to jump off the surface than if they were each a single adatom. If adatoms continue to cluster around the original adatom, at some point the cluster will be large enough that it is statistically unlikely for the entire cluster to "dissolve" back to the original state [50]. The formation of such a cluster on the surface is referred to as 2D nucleation, since adatoms can continue to increase the size of the cluster and the crystal. Higher supersaturations will increase the number of clusters that form and speed the growth of the crystal.

Step ledge growth can now be considered for the cluster of adatoms. If there is a ledge of atoms on the surface, an adatom may diffuse to the ledge because it will have more neighboring atoms to bond to and thus will be more likely to stay on the surface (see Figure 2.1). Particularly in vapor solid growths, surface diffusion is important for the step ledge growth to occur [50]. If there is a kink in the ledge, the adatom will have even more neighbors to bond to, and additionally, the adatom will not increase the surface energy[49, 50]. Once the ledge grows to the edge of the crystal, however,

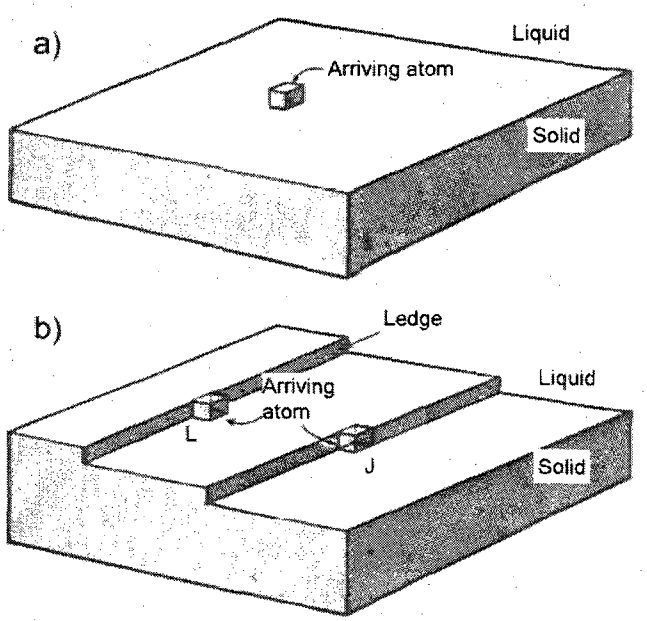

Figure 2.1: a) Adatom on a smooth crystal plane. This atom is weakly bound and may jump off the surface or diffuse across the surface. b) L is an atom attached to a ledge. J is an atom attached to a jog, or a kink, in the ledge (This figure is from Porter and Easterling [49]).

there are no readily accessible locations for more atoms to be added. The continued growth of the crystal depends on a sufficient number of atoms adsorbed onto the new surface to form another ledge.

What if the supersaturation is not sufficient to cause a cluster of atoms to form? Dislocations, particularly screw dislocations, in the existing crystal can be a step-ledge site for new atoms to adhere to [51]. A screw dislocation creates a ledge that will spiral upwards as more and more atoms are added to the ledge (see Figure 2.2). If the Burger's vector of the dislocation is large, the central part of the screw will be considerably strained. If the Burger's vector is very large, atoms will not occupy the center portion of the screw dislocation in order to relieve the strain, even though this means accommodating the additional surface energy [52]. Additionally, the step ledges have a tendency to bunch together as the ledges spiral around [50]. Step

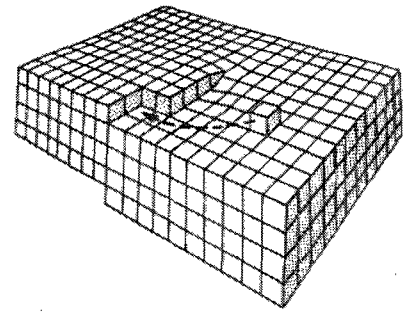

Figure 2.2: The screw dislocation causes the ledge to spiral around the crystal. (This figure is from Porter and Easterling [49])

bunching can create steps several atomic layers thick.

Another concept related to crystal growth is surface roughening. Burton, Cabrera, and Frank had some concept of surface roughening. They knew that at low temperatures step ledges would have lower kink densities than at higher temperatures [51]. This has since been observed as both geometrical and round shaped spirals around screw dislocations [9]. Round spirals have rough steps with a high kink density. This allows the step to advance in all crystallographic directions. Geometrical spirals have smooth-edged steps and a symmetry that follows the symmetry of the face. For example, (0001) SiC spirals can be either triangular or hexagonal as both shapes follow the symmetry of the (0001) face [9]. Surface roughening is found in three dimensions as well [53]. When cubes of NaCl are at equilibrium with the surrounding vapor above the roughening temperature, the corners and edges of the cube round off [54]. Jackson added to the discussion of surface roughening with the introduction of the α factor. The Jackson α factor assigns an approximate value for the relative surface roughness of various materials [55].

Another method of crystal growth is described by chemical vapor transport (CVT). CVT is where a gas picks up an atom in a high energy state on the surface of a solid and deposits it in a location on the solid where it will have a lower energy. ZnO and

InN nanowires have been reported to grow by a self catalyzed vapor transport process [56, 57].

2.4 Nanowire Growth used in this Study

Gallium nitride nanowires were grown by our collaborators at Howard University. They were formed by a direct reaction between elemental gallium and ammonia (NH_3) [58, 59]. Metallic gallium was placed on a boron nitride boat, which was then positioned in a quartz liner within the furnace tube. The furnace was then evacuated and 100 sccm of ammonia was flowed through the tube as the furnace was heated to 850°C, 950°C, or 1000°C. A matrix of GaN platelets forms on the quartz liner inside the furnace tube. Nanowires nucleate from active sites on the GaN platelets. The evolution of the matrix as a function of furnace temperature and growth time is a major contribution of this thesis and is discussed in Chapter 4.

Chapter 3

Characterization Methods

GaN nanowires and the matrix they grew from were characterized using a variety of methods. Each method gives different information about the GaN crystalline formations and their growth process. This chapter describes each method used to characterize the GaN crystals and explains what knowledge can be gained by using each method.

3.1 Transmission Electron Microscopy (TEM)

Transmission Electron Microscopes (TEMs) use an electron beam to image a very thin sample. The TEM takes advantage of the wave-like behavior of electrons to obtain high resolution images. From the Rayleigh criterion ($\sin(\theta) \approx 1.22\frac{\lambda}{D}$, where θ is the angular resolution limit, λ is the wavelength of light, and D is the diameter of the circular aperture), we know that the resolution of a microscope is limited in part by the wavelength used to form the image. Short wavelengths will give higher resolution than long wavelengths in otherwise identical systems. The wavelength of

an electron can be calculated by

$$\begin{aligned} \lambda &= \frac{h}{p} \\ &= \frac{h}{\sqrt{2m_0qV}} \frac{1}{\sqrt{1+\frac{2qV}{m_0c^2}}} \end{aligned} \tag{3.1}$$

where h is Plank's constant, p is momentum, m_0 is the mass of the electron, q is the charge of the electron, and V is the electric potential. The $1/\sqrt{1+\frac{2qV}{m_0c^2}}$ term is a relativistic correction which is necessary due to the high speeds of electrons in a TEM. The wavelength of an electron that has been accelerated by a 200kV potential (a typical TEM operating parameter) is 2.5pm, which is about five orders of magnitude smaller than the wavelength of visible light.

Within the column of a TEM, a beam of electrons is sent through the thin sample. The atoms in the sample diffract the electrons. When the diffracted electrons from one lattice plane have the same phase as the diffracted electrons from another lattice plane, the Bragg condition (given in 3.2) is satisfied and the waves will constructively interfere.

$$2d\sin(\theta) = n\lambda \tag{3.2}$$

A diagram of a TEM is given in Figure 3.1.

Depending on how the electro-magnetic lenses are focused, either the diffraction pattern or an interference pattern (the image of the sample) can be observed. High resolution TEM (HRTEM) can image samples at an atomic resolution. However, when looking at an HRTEM image, you are not "seeing" the individual atoms. HRTEM images are formed by allowing many diffracted beams as well as the transmitted beam to contribute to the image. When the beams are combined they constructively and destructively interfere, resulting in phase contrast. Phase contrast can be described

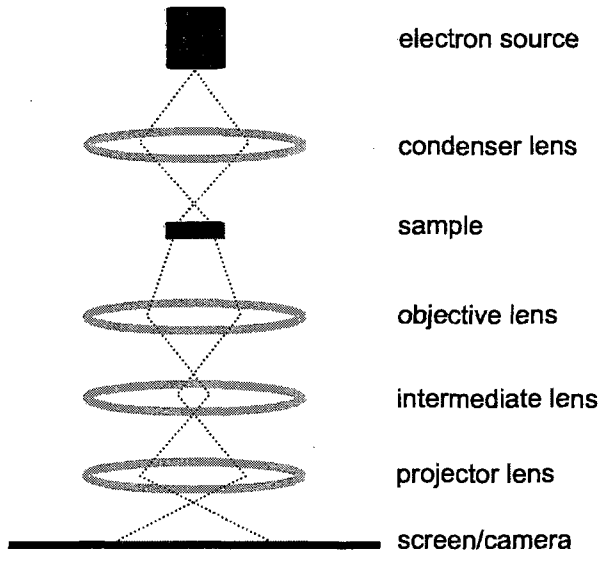

Figure 3.1: A diagram of the electron beam of a TEM going through the sample and a series of electro-magnetic lenses.

by [60]

$$T(\hat{u}) = 2A(\hat{u})\sin(\chi(\hat{u})) \tag{3.3}$$

where $\hat{u}$ is a reciprocal lattice vector. $A(\hat{u})$ is the aperture function and takes into account that an aperture placed after the objective lens will limit the number of beams used in forming the HRTEM image. $\chi(\hat{u})$ is the phase-distortion function and takes into account the fact that spherical aberration, astigmatism, and defocus affect the phase of each beam.

The diffraction pattern of a specific area of the sample can be obtained by putting an aperture around a selected area of the sample while in imaging mode, and then switching the TEM to diffraction mode. This technique is known as selected area electron diffraction (SAED). The resulting diffraction pattern can then be indexed to obtain the crystal structure of that particular area of the sample by comparing the relative distances and angles between the diffraction spots. The pattern can be thought of as the crystallographic structure in reciprocal space. This technique works

best when a single crystal is in the selected area, so that all the diffraction spots are from the same crystal orientation or phase.

Due to the spherical aberration of the objective lens, there is a limit to the size of the area that can be selected with an aperture [60]. In cases where the area of interest is too small to be imaged using SAED, a fast Fourier transform (FFT) can be applied to an HRTEM image of the area of interest to get a pattern similar to the SAED pattern. The Fourier transform switches between real space (x) and reciprocal space $\left(\frac{1}{x}\right)$, so the mathematical processing of the interference pattern of an HRTEM image results in the same pattern of spots that would be expected from an SAED of the crystal structure.

In this study, a JEOL 2200FS TEM was used to image the nanowires. The TEM is an important tool in the study of nanowire growth because it allows the crystalline structure and growth direction of the nanowires to be determined by solving the diffraction patterns and fast Fourier transforms (FFTs) of HRTEM images. The high resolution of the TEM allows the internal structure of the nanowires to be observed.

3.2 Scanning Electron Microscopy (SEM)

Scanning Electron Microscopes (SEMs) are similar to TEMs in that they also image samples with an electron beam. SEMs typically operate at around 15kV which means the wavelength of the electrons are approximately 9.7pm. Therefore SEMs have much better resolution than light microscopes, but lower resolution than TEMs. The main difference between a TEM and an SEM is that in a TEM the electrons go through the sample and in an SEM the electrons only interact with the surface of the sample. This means that sample preparation is generally much easier for SEM than for TEM because SEM samples do not need to be thin and electron transparent.

To take an SEM image, the electron beam is rastered across a selected area of

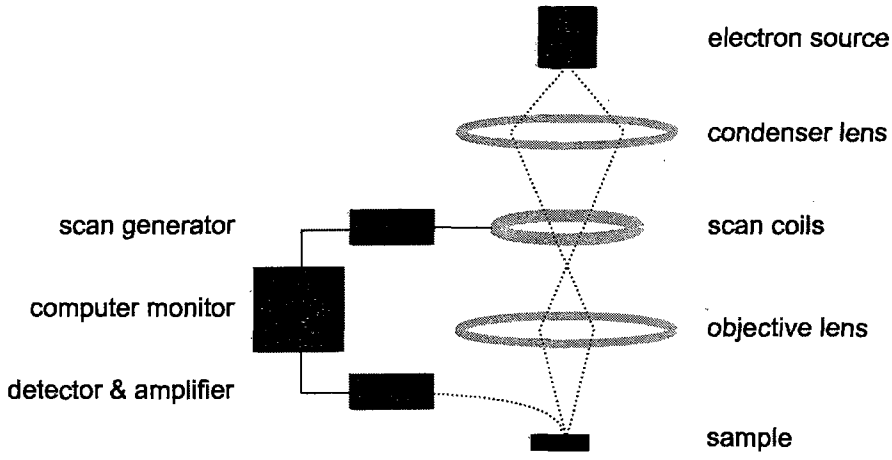

Figure 3.2: A diagram of the electron beam of a SEM going through a series of electro-magnetic lenses and interacting with the sample. Secondary electrons escape the surface of the sample and get detected.

the sample. The high energy electrons from the electron beam transfer some of their energy to electrons of the sample's atoms, causing the atoms to ionize. The electrons resulting from the ionization (called secondary electrons) have a low energy, which means they can only escape the sample if they are close to the surface of the sample. Electrons that escape the sample are accelerated toward a detector. As the electron beam is raster-scanned across an area of the sample, the number of electrons detected is translated into an intensity for each pixel on a computer monitor. Because electrons near sharp corners or edges can more easily escape the sample and get to the electron detector, SEM images have a 3D appearance. The basic mechanics of SEM operation is illustrated in Figure 3.2.

In this study a Hitachi S-4700 II Field Emission SEM was used to examine the differences in morphology of samples grown under different conditions. It was also used to characterize the size and shape of the nanowires as well as how the nanowires are connected to the growth matrix.

3.3 X-Ray Diffraction (XRD)

X-ray diffraction (XRD) is useful for determining the crystal orientations found near the surface of a sample. The sample is placed in a *goniometer* which can rotate the sample about multiple axes to precise angular positions. A beam of x-rays is directed to the surface of the sample and is diffracted according to Bragg's law (Equation 3.2). The intensity of the diffracted beam is then detected. This set-up is illustrated in Figure 3.3. The angle of the sample and the detector are changed relative to the x-ray source to determine which crystal planes diffract the strongest. For a plot of intensity vs. 2θ, the detector and sample are rotated simultaneously so that the x-ray source and the detector are at the same angle with respect to the detector (see Figure 3.4). When Equation 3.2 is satisfied, there will be a peak in intensity. Each peak is related to the distance between the diffracting planes. For cubic structures, the distance d between planes is given by

$$d = \frac{a}{\sqrt{h^2 + k^2 + l^2}} \tag{3.4}$$

where a is the length of the unit cell and h, k, and l are the Miller indices. The distance between planes for hexagonal structures is given by [31]

$$d = \sqrt{\frac{1}{\frac{4}{3}\frac{h^2 + hk + k^2}{a^2} + \frac{l^2}{c^2}}} \tag{3.5}$$

where a and c are axes of the unit cell. Thus a peak of x-ray intensity at a specific diffraction angle corresponds to the specific plane that is causing the diffraction. Not all planes cause a peak in the intensity. The structure of the crystal determines which planes cause peaks and which do not. This is characterized by the structure factor. For a calculation of the structure factor of zinc-blende and wurtzite GaN, see the appendix.

Pole figures relate the relative intensity of the detected x-rays to the crystal orientation near the surface of the sample. This is done by rotating through ϕ and incrementally changing χ while keeping the 2θ angle constant. If the observed peak intensities do not change as a function of beam-sample orientation, the sample surface does not have a preferred orientation.

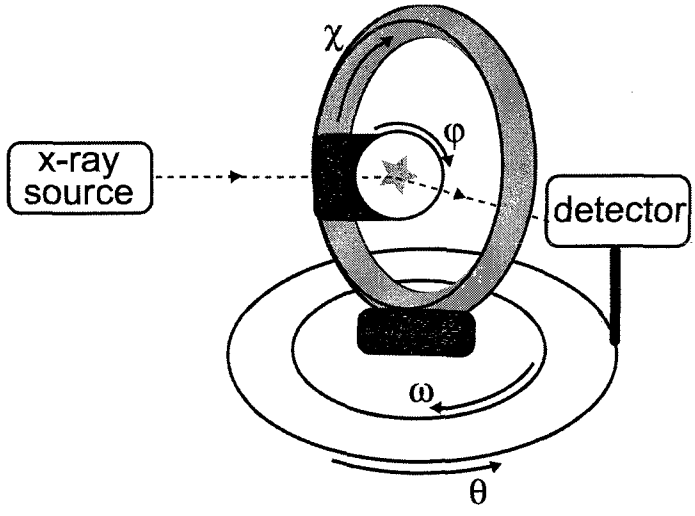

Figure 3.3: The sample (illustrated as a star) is held in a goniometer. The sample diffracts the x-rays, and the intensity of the x-rays is measured by the detector.

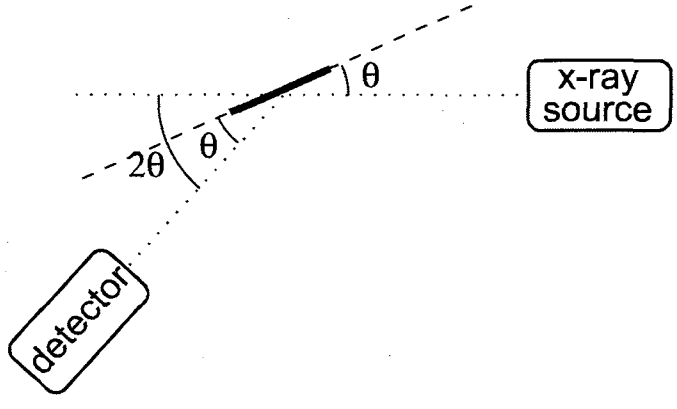

Figure 3.4: The geometry of a 2θ scan.

Chapter 4

Results

The effect of temperature on GaN nucleation and nanowire growth was investigated at furnace growth temperatures of 850°C, 950°C, and 1000°C. From previous studies [61, 62] it is known that nanowires grown from 850°C and 950°C have both wurtzite and zinc-blende crystalline domains along the entire length of the nanowire. The growth direction is $\langle 11\bar{2}0 \rangle$ for the wurtzite domains and $\langle 110 \rangle$ for the zinc-blende domains. However, the majority of the nanowires and rods grown at 1000°C are pure wurtzite with a $\langle 0001 \rangle$ growth direction.

4.1 Matrix Growth and Evolution

In order to understand why the growth orientation changes as a function of temperature and how nanowires with multiple phases form, it is necessary to understand what kind of environment the nanowires are growing in. Thus an in-depth study of the growth matrix was carried out. The matrix, like the nanowires, forms from the direct reaction of gallium with ammonia. A better understanding the formation mechanisms of the matrix will also lead to a better understanding of the nanowire growth.

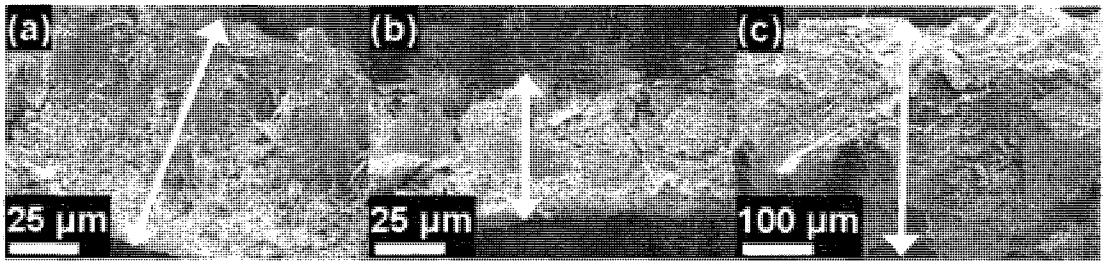

Figure 4.1: (a), (b), and (c) are SEM images of the side view of the matrix growth at 850°C, 950°C, and 1000°C, respectively. The approximate thicknesses of the samples, indicated by the arrows, are (a) 87µm, (b) 53µm, and (c) 339µm.

4.1.1 SEM of Matrix Cross Sections

The matrix growth and evolution was investigated at the micron scale by imaging cross sections of the matrix in the SEM. Matrix cross sections were prepared by natural fracture so that the sample could be viewed edge-on in the SEM. The thicknesses of each sample is given in Figure 4.1, although it should be noted that the thickness of each sample varied widely. All SEM images of the matrix cross sections are oriented so that the top of the image corresponds to the "top" of the sample, except Figure 4.1a, where the matrix is shown at an angle. In both the 850°C and 950°C growths, distinct changes in the matrix morphology were observed between the top and bottom surfaces of the matrix, however, such changes in morphology were not observed in the 1000°C growth.

The matrix grown at 850°C is shown in detail in Figure 4.2b and exhibits distinct layers of different platelet morphologies. The bottom-most layer (labeled Layer 1) of the matrix consists of thin bent sheets of GaN, and therefore has a lighter contrast than other regions of the cross section. The next layer (Layer 2) of the matrix has small formations with rounded edges. The layer above that consists of relatively large hexagonal plates and resembles matrix formations on the top surface of the 1000°C growth (discussed later in this chapter). From the cross section, it appears that the

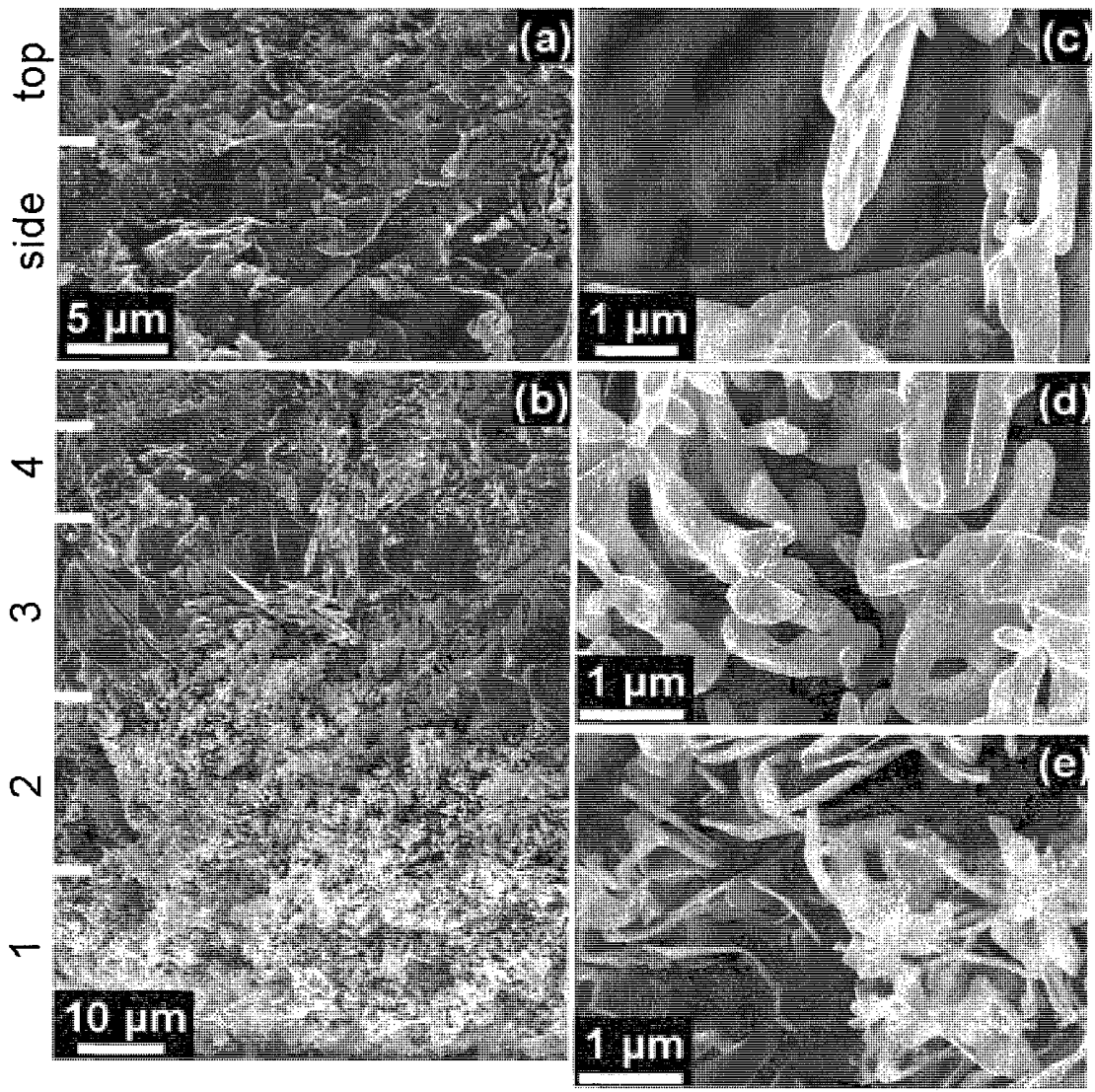

Figure 4.2: Side view of matrix growth at 850°C. (a) Comparison of the side view and top view of the uppermost matrix formation type. (b) Layered growth at 850°C. Lines and labels on the left side of the picture mark the boundaries between the different matrix layers. (c), (d), and (e) Close-up images of layers 3, 2, and 1, respectively.

large platelets prefer to be vertically oriented. Close-up images of Layers 3, 2, and 1 of this matrix are shown in Figure 4.2c, d, and e.

The upper most layer of the 850°C matrix, which corresponds to the nanowire growth surface, consists of small platelets with sharp corners. A close-up of the upper most layer of the matrix is shown in Figure 4.2a, where the line on the left side of the image marks the boundary between the top surface and the cross section of the top matrix region. While some of the large platelets appear to penetrate the surface (this can also be seen in an SEM of the top surface in Figure 4.5), the majority of the surface consists of the smaller platelets. It is unclear exactly why small crystals would form on top of the larger platelets. It is possible that the larger crystals were etched or otherwise decomposed to form the top layer of small crystals. N_2 is known to be a carrier in chemical vapor transport mechanisms and could be present in the growth furnace from dissociated ammonia [63].

The cross section of the 950°C growth showed three different layers of matrix growth (Figure 4.3b). The top layer (layer 3) appeared to be composed of small crystallites with relatively sharp edges (Figure 4.3a and c), similar to the top layer of the 850°C growth. Layer 2, pictured in Figure 4.3d, had distinct, rounded formations that appear similar to the layer of 850°C growth shown in Figure 4.2d. The size and shapes of the matrix in the bottom layer (Figure 4.3e) are comparable to those in layer 2, but they are more densely packed.

It is interesting to note that the top surface of both the 850°C and 950°C are similar, even though in the 850°C growth the top layer forms on large crystals, and in the 950°C growth the top layer forms on small rounded crystals. The 950°C growth appears to skip the large crystal growth altogether and jump directly into the small crystal formations from which the nanowires nucleate. Alternatively, it may be possible that the large crystals did form, but were etched more quickly than those of the 850°C to create the small crystals.

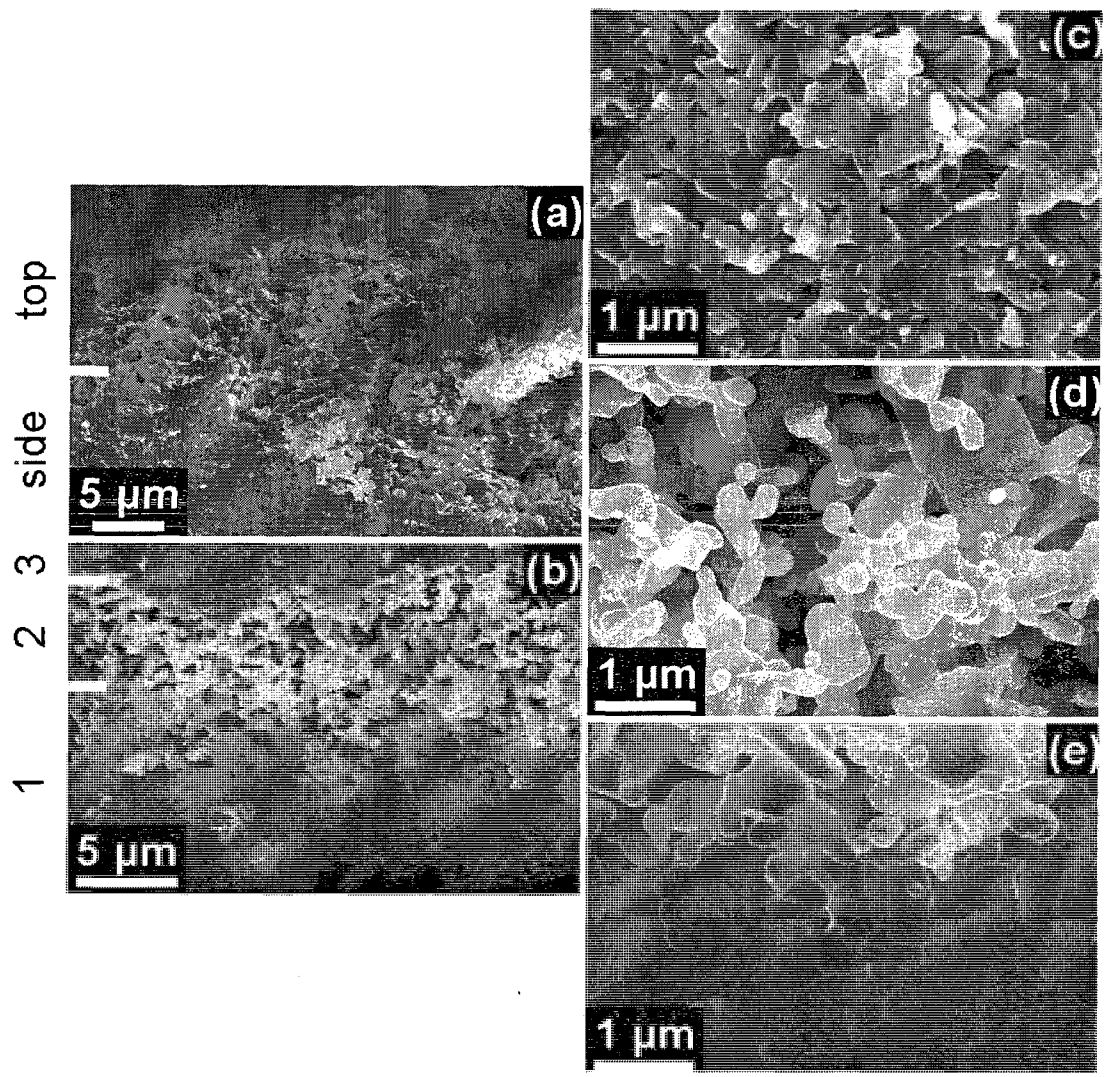

Figure 4.3: Side view of matrix growth at 950°C. (a) Comparison of the side view and top view of the uppermost matrix formation type. (b) Layered growth showing three different matrix formation types. (c), (d), and (e) Close-up images of layers 3, 2, and 1, respectively.

The cross sectional view of the 1000°C sample did not show any evidence of layered platelet morphologies. Relatively large crystal domains were present from the top to the bottom of the sample (see Figure 4.4a). However, interesting formations were observed. Figure 4.4d shows a number of holes formed in one portion of the sample near the bottom of the matrix. Most of the cross section had structure that was similar to that shown in Figure 4.4c, which was imaged near the middle of the cross section. Hexagonal pits were observed near the top of the sample (see Figure 4.4b). The bottom of the hexagonal pits appear to be flat. These pits could have come about by an etching process, since it seems unlikely that the matrix selectively grew around the pits.

4.1.2 SEM of the Top Surface of the Matrix

Nucleation sites for nanowires are found on the top surface of the matrix for all three growths. Nanowires were also observed on the bottom surface in the 1000°C growth, and will be discussed later. SEM images of the top surface for each of three matrix samples grown at 850°C, 950°C, and 1000°C are shown in Figure 4.5. The matrix morphology was observed to change as a function of growth temperature, and an abrupt change occurs in the growth mechanism between 950°C and 1000°C.

The 850°C and 950°C matrix formations were similar and consisted of approximately 1µm sized platelets. Nanowires growing from this type of matrix had a cross-sectional width of 50nm to 250nm. Note that a few larger crystals with lengths on the order of 10µm emerge through the surface of the 850°C growth on the left hand side of Figure 4.5a. These larger sized crystals were never observed at the 950°C growth, and this observation is confirmed by the matrix cross sections. The nanowires appear to grow from the edges of the platelets and have triangular cross sections.

At 1000°C three different types of matrix were observed. Type 1 had relatively large 1-20µm crystallites of GaN. A few large rods with widths between 0.5µm and

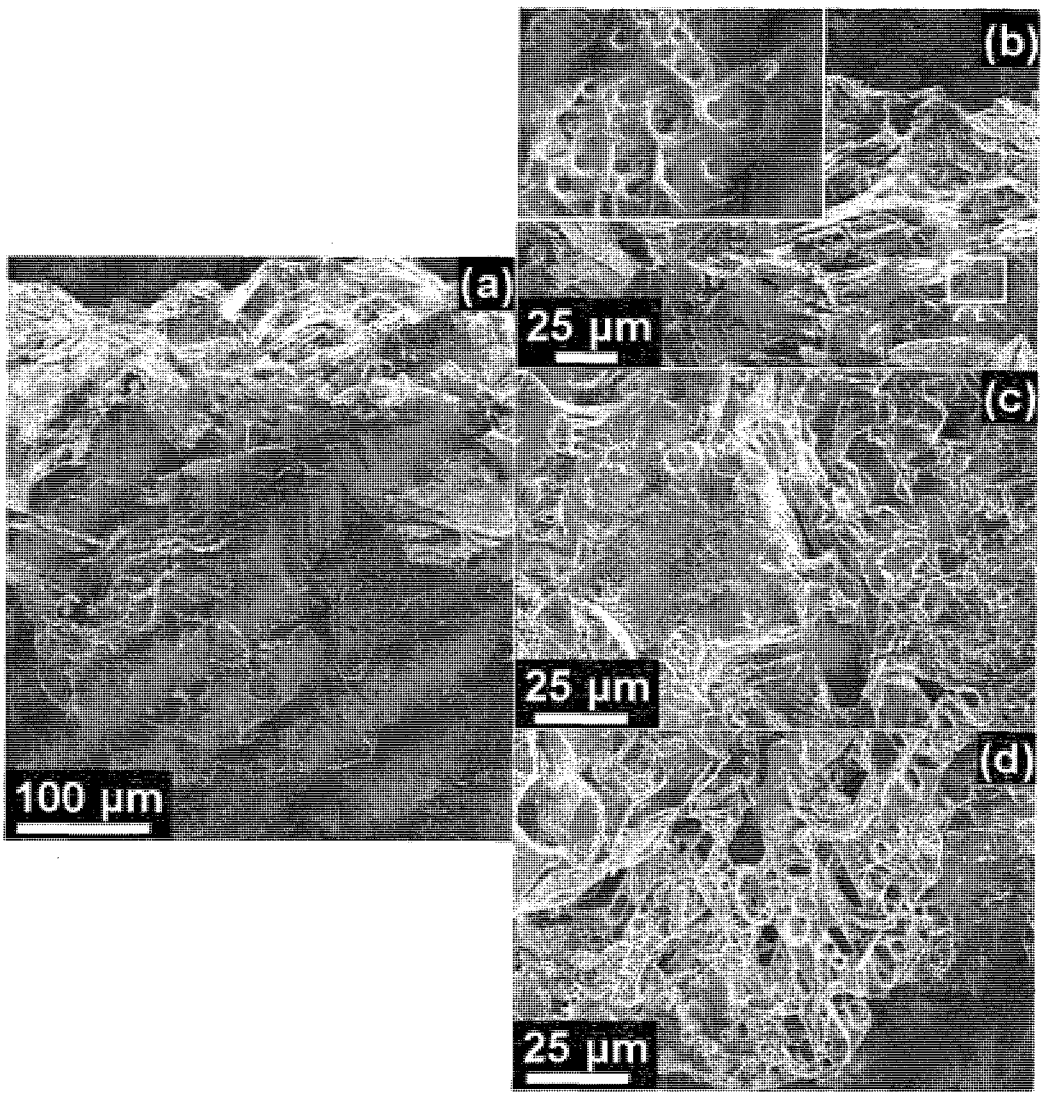

Figure 4.4: (a) Side view of the 1000°C growth. (b) Close-up of the top portion of the cross section. Inset shows hexagonal pits. (c) Middle portion of the sample. (d) Holes near the bottom of the sample.

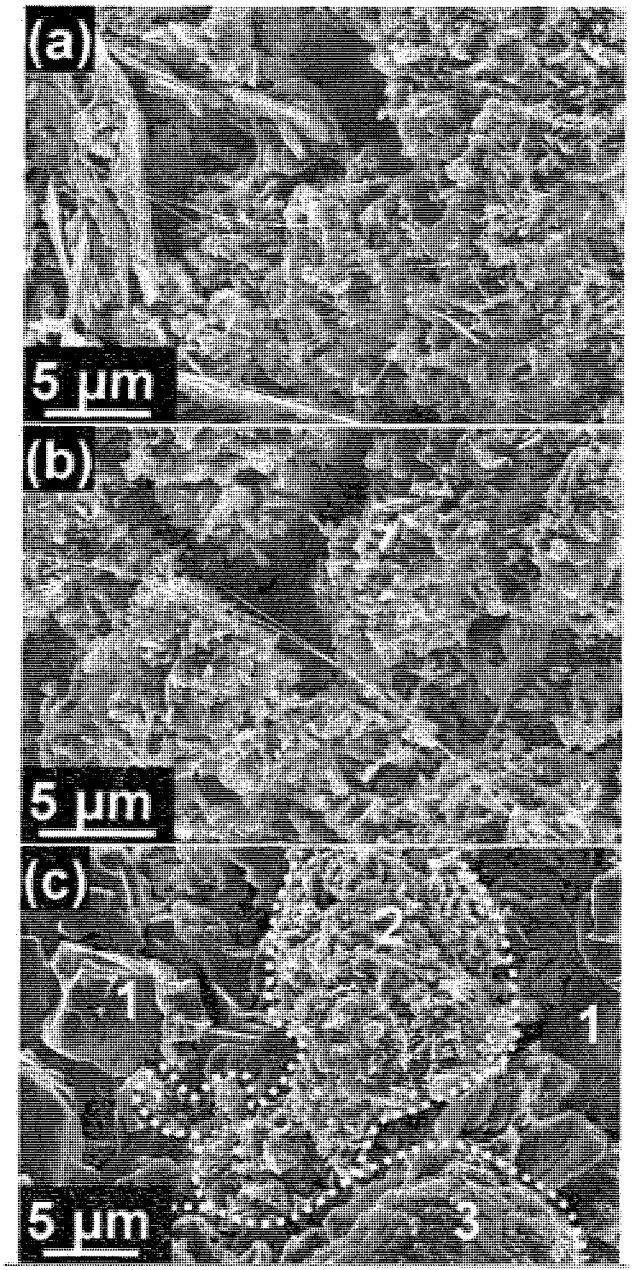

Figure 4.5: SEM images of typical GaN matrix and nanowire growth. (a) SEM images of typical 850°C growth showing several nanowires growing from the matrix (b) SEM images of typical 950°C growth. (c) Matrix growth at 1000°C. Type 1 matrix consists of large GaN crystallites, Type 2 matrix consists of medium-sized platelets with sizes on the order of 1 µm, and Type 3 matrix consists of small platelets on the order of 0.1 µm.

30μm formed from the Type 1 matrix. These rods have a hexagonal cross section, and no wires with diameters less than 100nm were observed growing from these parts of the matrix. Because of the hexagonal cross section, these rods grow in the ⟨0001⟩ direction, and this has been confirmed by TEM. Type 2 matrix had medium sized 0.1-1μm platelets. The Type 2 matrix growth appeared to be comparable to the matrix for 850°C and 950°C and also had similar nanowire nucleation. Type 3 matrix consisted of small platelets around 50-300nm wide and the platelets were typically clustered in spherical mounds. NW growth was also observed from the Type 3 platelets. These nanowires also had a triangular cross section, suggesting that the growth mechanism may be the same as the nanowires that grew at 850°C and 950°C. Specific nucleation sites for nanowires and rods will be discussed in Section 4.2.1. The remainder of this section will continue to focus on the growth and morphology of the matrix.

4.1.3 SEM of the Bottom Surface of the Matrix

The bottom side of the matrix (the side that formed on the quartz tube in the growth furnace) was also imaged using the SEM to study the evolution of the matrix. In Figure 4.6, the top and bottom sides of two pieces of matrix from the 850°C growth were placed side by side to be imaged. The morphology of the matrix on both surfaces were similar, however, nanowires were only observed on the top surface of the matrix.

The bottom surface of the 1000°C growth is every bit as complex as the top surface. A wide angle view of the bottom surface (Figure 4.7a) shows that multiple matrix formations are present and that rod growth is possible. Near the base of the rod, nanowires were also observed (Figure 4.7b). Nanowires were observed to originate from areas of the matrix with smaller crystallites, as shown in Figure 4.7c. Some of these nanowires had nodules on them, which may indicate the beginning of dendritic growth.

One of the matrix regions on the bottom surface of the 1000°C growth looks like

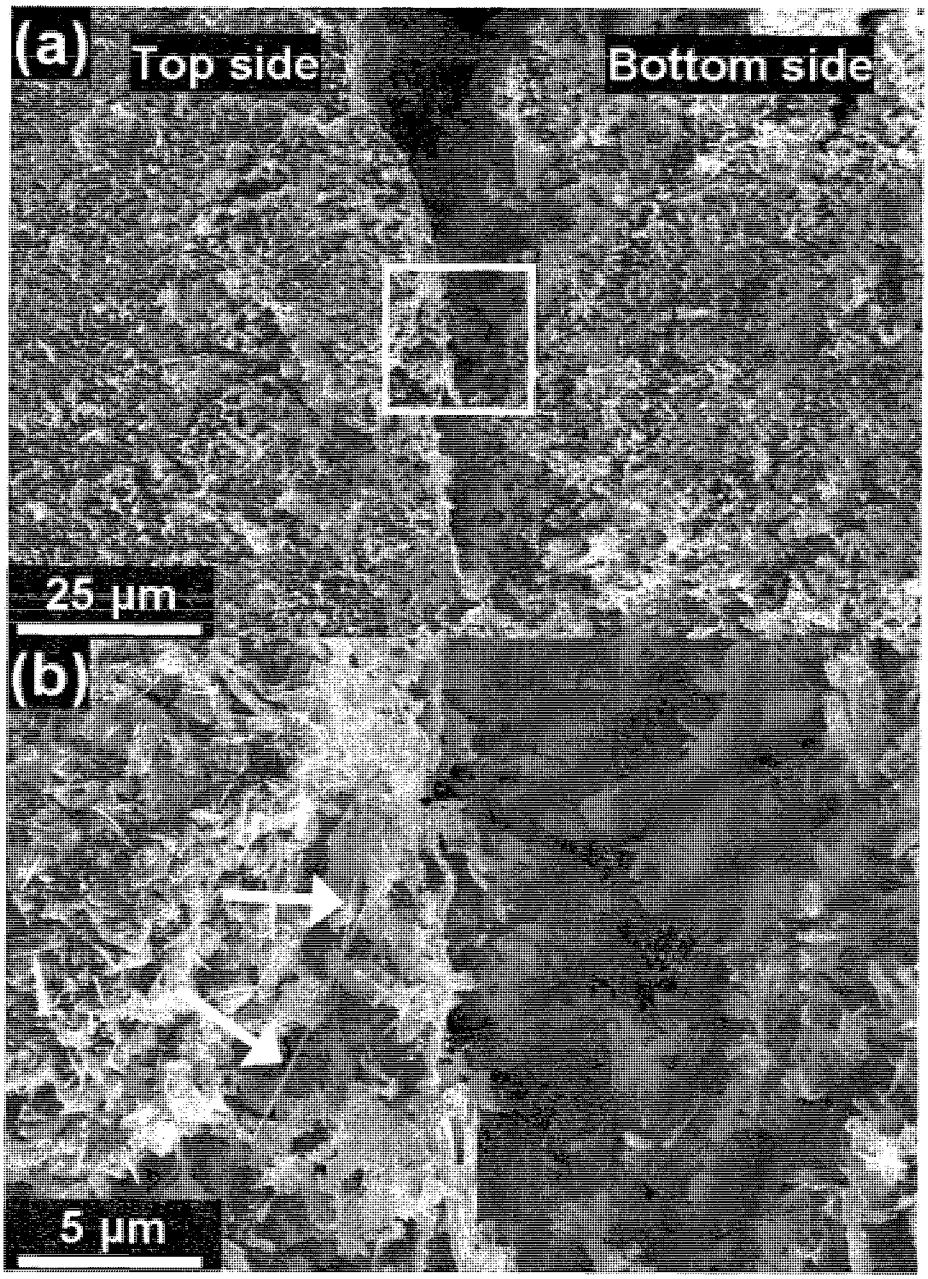

Figure 4.6: (a) Matrix morphology of the top and bottom surfaces of the 850°C growth are similar. (b) Close-up of the boxed area in (a). Arrows point to nanowires on the top surface. No nanowires were observed from the bottom surface.

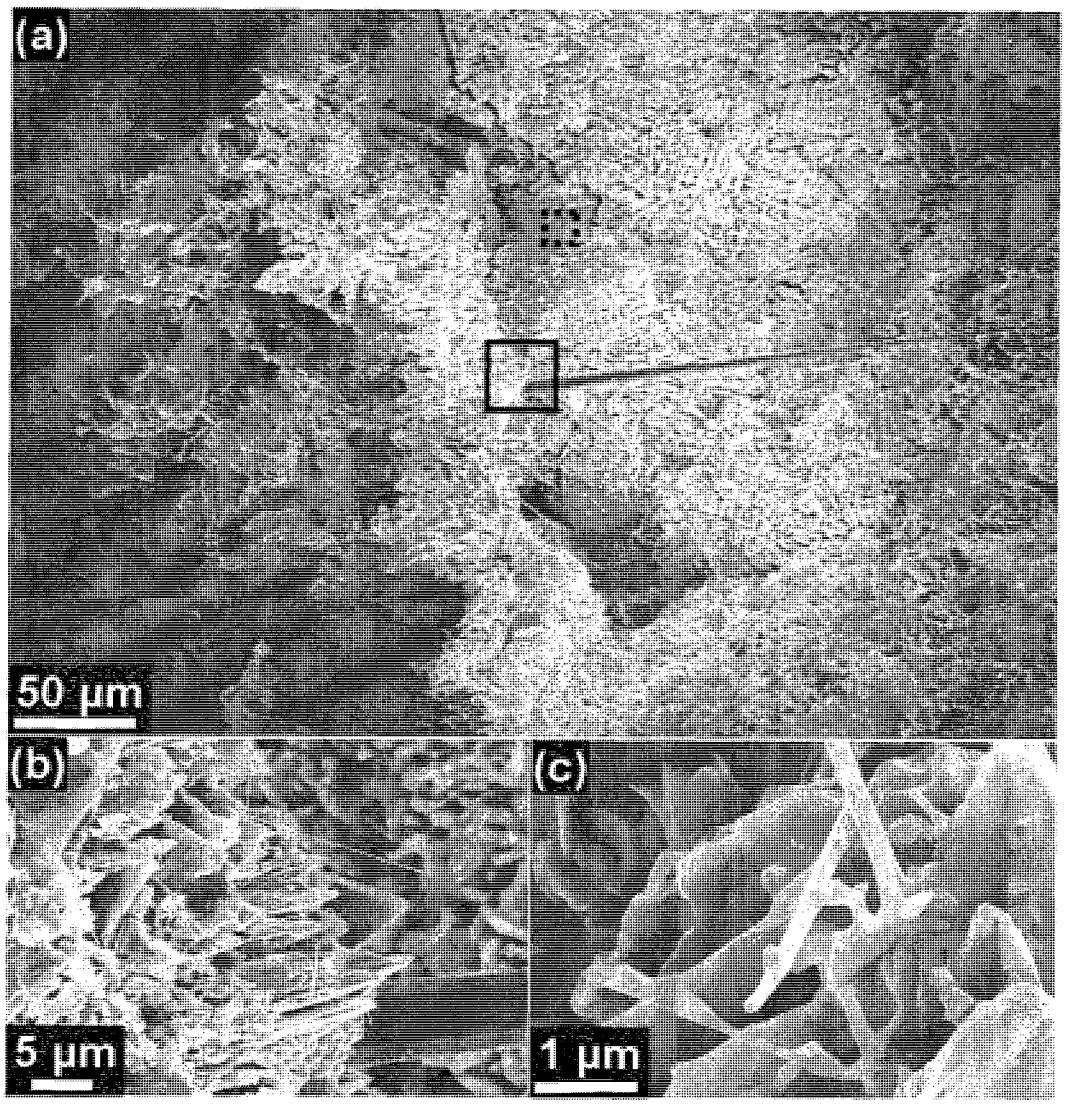

Figure 4.7: (a) A wide angle view of the bottom surface of the 1000°C growth. The area in the solid square is shown in (b) and contains nanowire growth near the base of the rod. The area in the dotted square is shown in (c) and contains nanowire growth.

the top surface of the 1000°C growth. SEM images of these regions are shown for comparison in Figure 4.8a and b. Hexagonal rods and medium and large crystallites comparable to the Type 2 and Type 1 matrix described in Figure 4.5 were observed on both the top and bottom surfaces. Nanowires were also observed to originate from the medium platelets of both the top and bottom surfaces. A different region of the bottom surface resembles matrix formations observed in the cross section of the 1000°C matrix. SEM images of these regions are shown for comparison in Figure 4.8c and d. Neither of these regions has a clearly defined platelet structure and a number of holes are evident in both images. It may be possible that part of the bottom surface broke off during sample preparation, revealing the matrix structure of the center of the matrix instead of the true bottom surface.

Another region of the bottom surface had a unique structure not observed on any other sample. This region is composed of 2-10 μm domains of platelets which are all oriented in the same direction. SEM images of this matrix formation is shown in Figure 4.9.

4.1.4 XRD of the Matrix

Nanowires grown at 850°C and 950°C contain zinc-blende crystalline domains. Therefore, the growth surface of the matrix was carefully investigated to determine if it had any significant portion of zinc-blende crystal structure to serve as a nucleation site. XRD provides information about the crystal structure near the surface of the sample, since the x-rays only penetrate a few microns into the sample. Intensity peaks occur for planes with allowed Bragg reflections, as determined by the structure factor (see the Appendix for details of the structure factor calculation for zinc-blende and wurtzite GaN). Most of the zinc-blende peaks occur very close to wurtzite peaks. The exception is the (002) zinc-blende peak at 39.8°, which makes it the main marker for detecting the presence of zinc-blende.

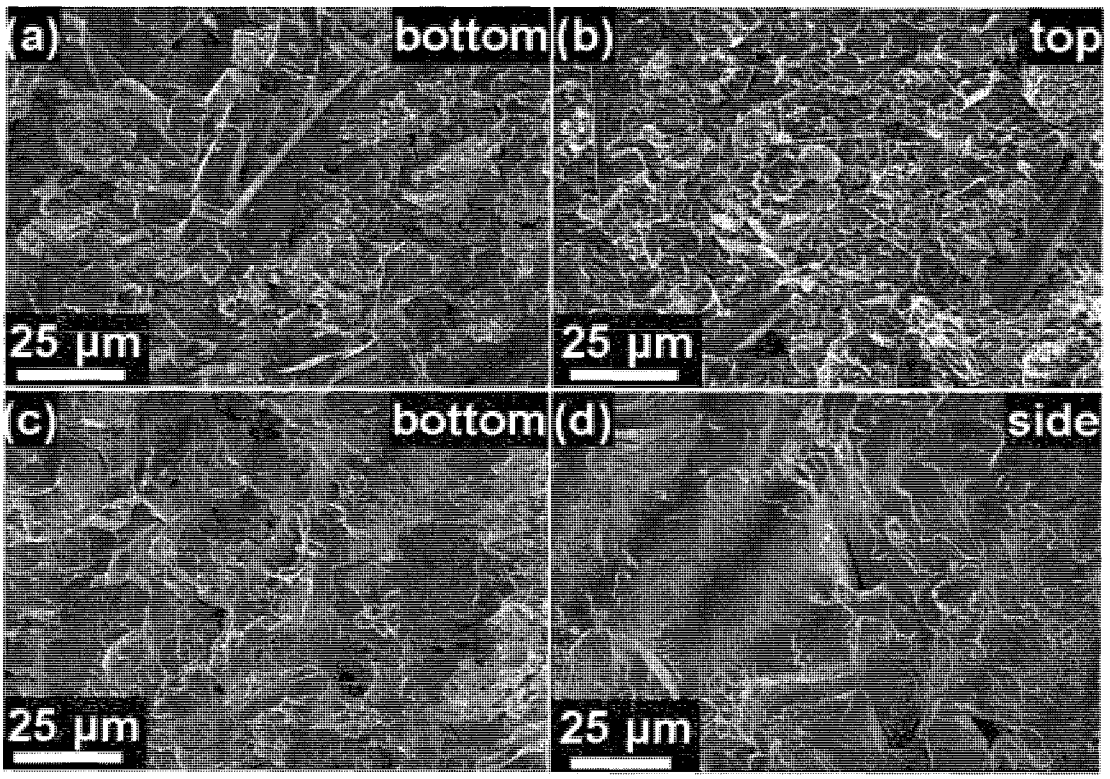

Figure 4.8: (a) and (c) Two different areas on the bottom surface of the 1000°C growth. (b) The top surface of the 1000°C growth is comparable to (a). (d) The cross section of the matrix is comparable to (c).

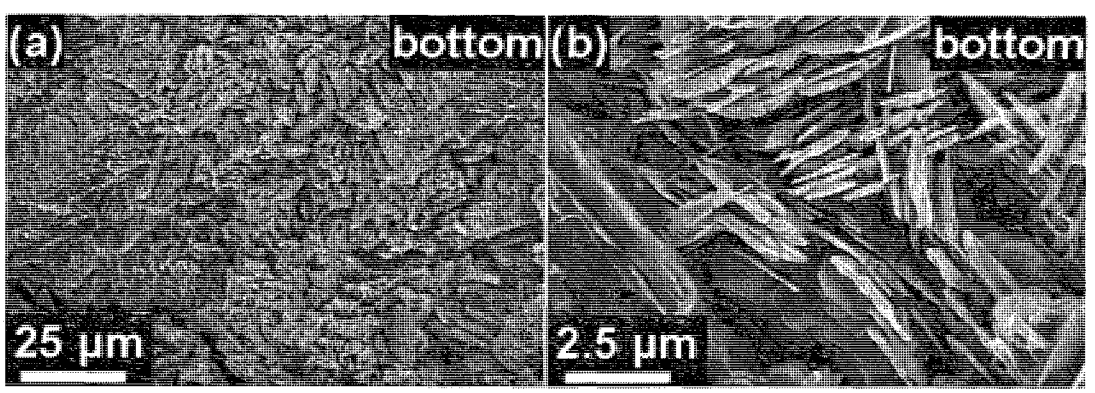

Figure 4.9: (a) Region of unique matrix formation on the bottom of the 1000°C growth. (b) Close-up of (a).

Relative intensities of powder diffraction for wurtzite and zinc-blende GaN are plotted in Figure 4.10 [5, 6]. The relative intensities of zinc-blende GaN had to be obtained from recent literature instead of from the standard reference of the powder diffraction files because zinc-blende GaN is an uncommon material. An ideal powder diffraction sample has small crystal particles with completely random orientations. A sample containing crystals with a preferred orientation will have different relative peak intensities than a sample with random orientations [64]. Data from the 2θ scan of the sample grown at 850°C is also plotted in Figure 4.10. The relative peak intensities from the 850°C sample are close to the relative intensities for powder diffraction from wurtzite GaN, suggesting that the GaN platelets on the sample surface are randomly oriented. A pole figure was taken of the 850°C sample, which also suggested that the platelets were randomly oriented and the surface of the sample has no texture.

X-ray diffraction (XRD) of the growth surface of each of the three samples reveals that the matrix is predominantly wurtzite. The 2θ scans for each of the three samples are compared in Figure 4.11. Silver epoxy was used to adhere the GaN samples to a steel puck, so peaks from silver and iron are apparent in the 2θ scans. A 2θ scan of just the epoxy and steel is also shown in Figure 4.11 for comparison. There was not enough of the zinc-blende structure over the surface of the sample to form a significant peak at 39.8°. We therefore conclude that the growth surface is predominantly wurtzite. This finding is important as it establishes that there is no evidence for a zinc-blende nucleation site for the homoepitaxial growth of the zinc-blende domains within the nanowires.

4.1.5 TEM of the Matrix

FFTs of HRTEM images of growth matrix platelets further confirm that the platelets are wurtzite. The platelets may have smooth sides and sharp corners (Figure 4.12a) or nanoscale ledges on the sides (Figure 4.12b-d). Smooth sides and nanoscale ledge sides

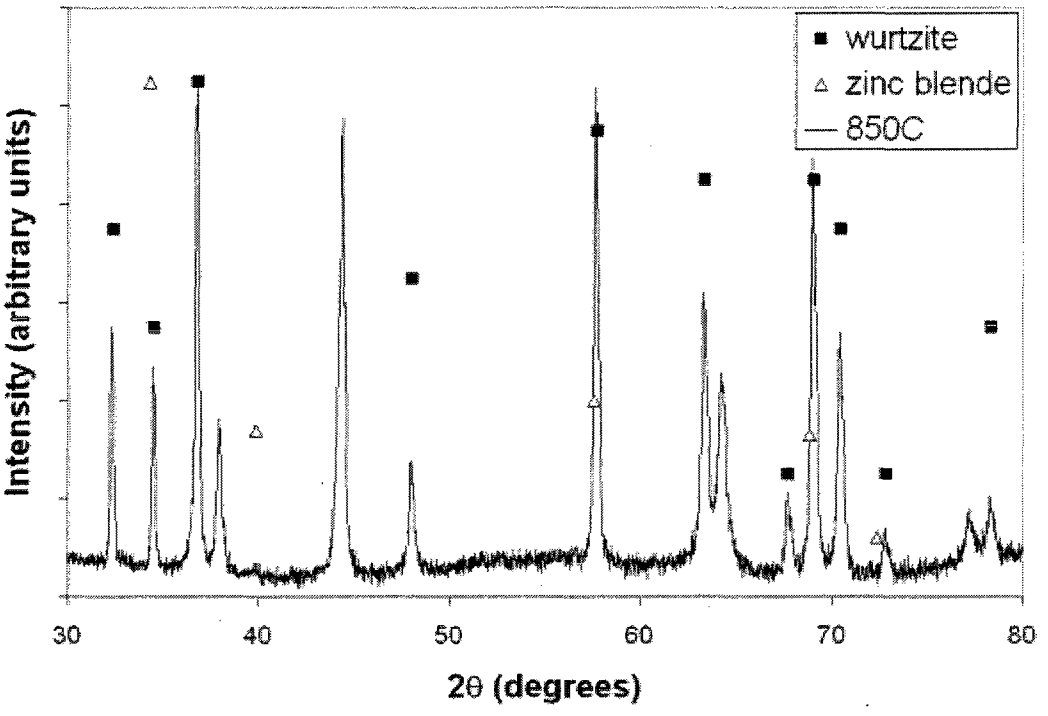

Figure 4.10: Relative intensities of each peak for powder diffraction of wurtzite [5] and zinc-blende [6] GaN. The 2θ scan of the 850°C sample is included for comparison.

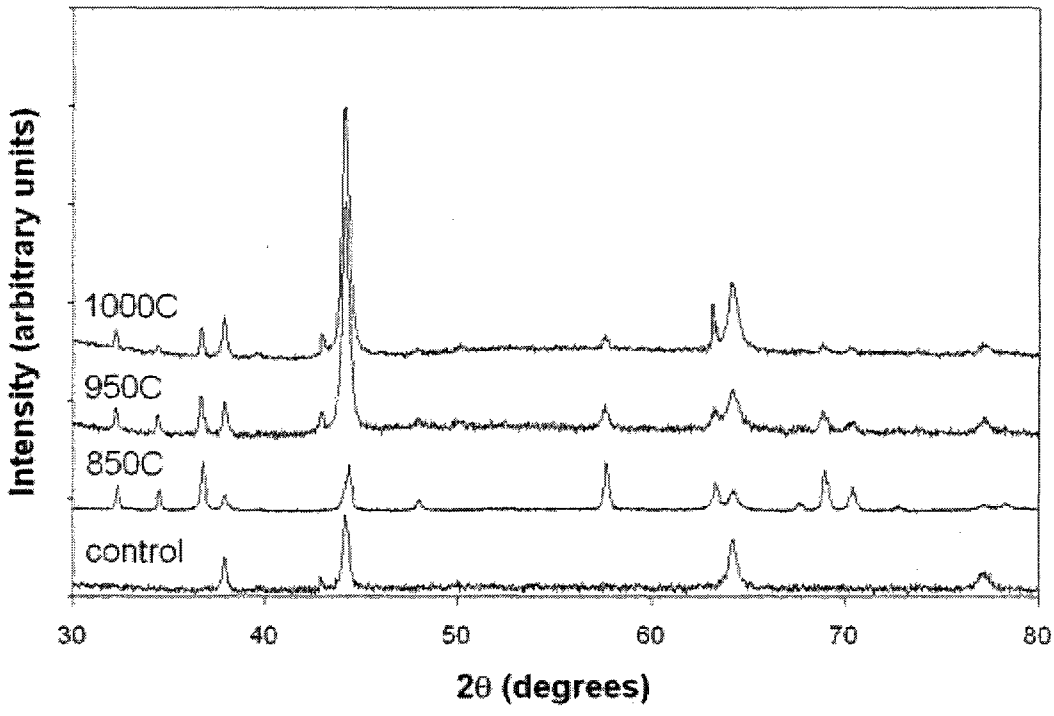

Figure 4.11: 2θ scans for each growth temperature. The control sample was the steel puck and silver epoxy used in the sample preparation.

may be present on the same platelet. The nanoscale ledges are 10-30 nm wide and, judging from the electron transparency, on the order of tens of nanometers thick. The nanoscale ledges are triangular with $\{10\bar{1}0\}$ sides, and an apex pointing in a $\langle 11\bar{2}0\rangle$ direction. Some platelets had apparently decomposed in the $[11\bar{2}0]$ direction. This decomposition occurred both at the platelet level (Figure 4.12c), where the corners are rounded instead of faceted, and at the nanoscale ledge level (Figure 4.12d), where a $\{11\bar{2}0\}$ plane could also be exposed. From the size of the platelet shown in Figure 4.12c, it is likely that the platelet came from the Type 2 matrix of the 1000°C growth.

4.2 $\langle 11\bar{2}0\rangle$ Nanowire Nucleation and Growth

Orientation change, single phase vs. multiphase, and cross sectional width and shape are the main points of differentiation between nanowires and rods. This section deals with nanowires that grow in the $\langle 11\bar{2}0\rangle$ direction and are typically multiphase with a triangular cross section 30-250 nm in width. This type of nanowire growth is the predominant form of nanowire growth at 850°C and 950°C. This type of nanowire also grows at 1000°C from similar growth matrix surfaces.

4.2.1 SEM of $\langle 11\bar{2}0\rangle$ Nanowires

Nanowires from the 850°C and 950°C growths are oriented with the axis of the wire in the $[11\bar{2}0]$ (wurtzite) and [011] (zinc blende) directions, as demonstrated by TEM (shown later). SEM images of these growths show that the nanowires originate from the sides of the wurtzite platelets and the $[11\bar{2}0]$ growth direction can often be inferred from the images. Close-up images of nanowire base and tip morphologies are shown for all three temperatures in Figure 4.13. Nanowires with triangular cross sections were observed in the 850°C and 950°C growths, as well as the Type 3 matrix at 1000°C. This can be seen in Figure 4.13 (b) and (f). In Figure 4.13(a), the nanowire

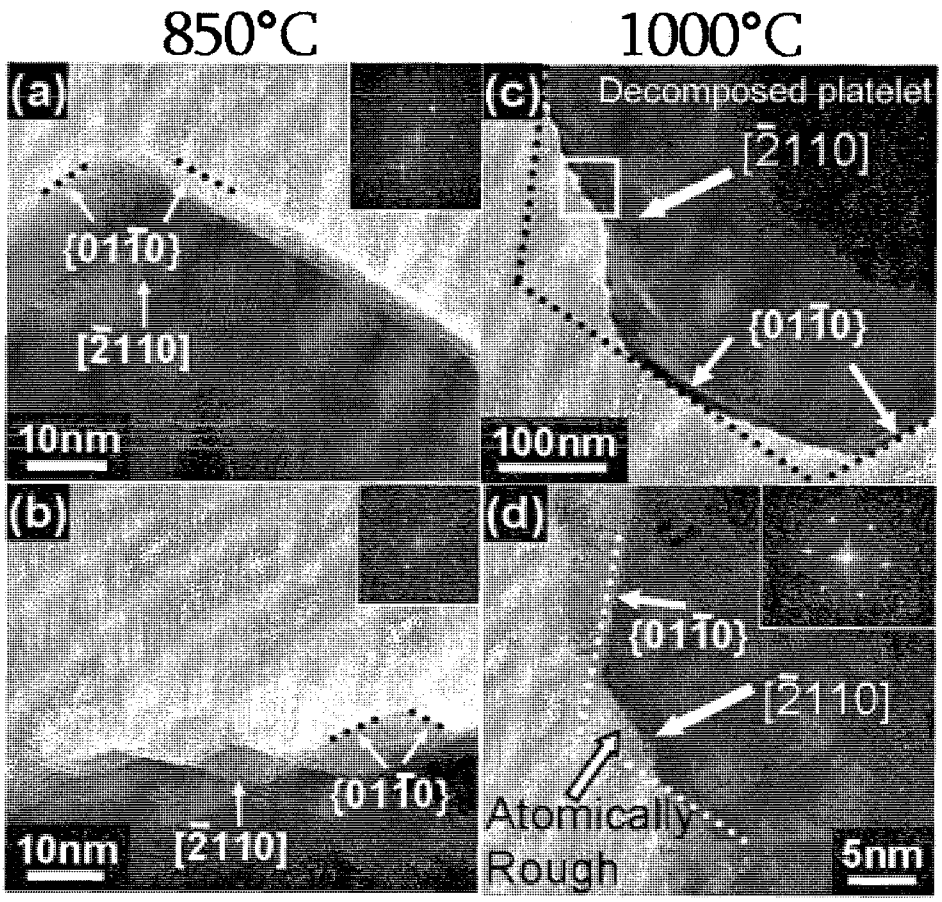

Figure 4.12: TEM of the matrix platelets. (a) A platelet grown at 850°C with smooth sides. (b) A platelet grown at 850°C with nanoscale ledges. (c) A platelet grown at 1000°C which has decomposed at the corners. (d) Close-up of the area indicated in (c). (Figure adapted from pictures published in Nanotechnology [7].)

(grown at 850°C) appears to originate from several layers of the matrix. Similar nucleation sites were observed in the 950°C growth and in the Type 2 matrix 1000°C growth. The nucleation sites shown in Figure 4.13(c) and (d) appear to come out of the edges of the platelets. On both of these nanowires, a thin fin appears to be attached near the base of the nanowire, indicating competitive growth in the $\langle 10\bar{1}0 \rangle$ direction. In GaN thin films, the $\langle 11\bar{2}0 \rangle$ direction is the fastest growth direction, and $\langle 10\bar{1}0 \rangle$ is the second fastest direction. In the case of these nanowires, the growth rates in the $\langle 11\bar{2}0 \rangle$ and the $\langle 10\bar{1}0 \rangle$ directions compete, and the $\langle 11\bar{2}0 \rangle$ growth eventually dominates so much that a nanowire is formed instead of a platelet. Similar nucleation sites were also observed in the 850°C growth.

Nanowires grown from the Type 3 matrix are shown in Figure 4.13(e) and (f). It is not known for certain what growth direction these nanowires have, but the $\langle 11\bar{2}0 \rangle$ direction is likely because of the triangular cross section. Additionally, a single phase nanowire grown in the $\langle 11\bar{2}0 \rangle$ direction was observed in the TEM for the 1000°C growth, so it is possible that the nanowires from the Type 3 matrix formations are single phase.

4.2.2 TEM Nanowire Cross Sections: Nanowires as a Nucleation Mechanism Diagnostic

Cross sectional HRTEM of the nanowires was performed in order to obtain information of the internal crystal structure of the nanowires. These samples were prepared using a focused ion beam (FIB) to mill a thin slice from the center of the wire, and the details of this procedure are described elsewhere [7, 8]. Nanowire cross sectioning and HRTEM was performed by B. W. Jacobs; however the analysis of the 950°C cross section is a new contribution of this thesis.

A cross section of a nanowire grown at 850°C is shown in Figure 4.14. Multiple

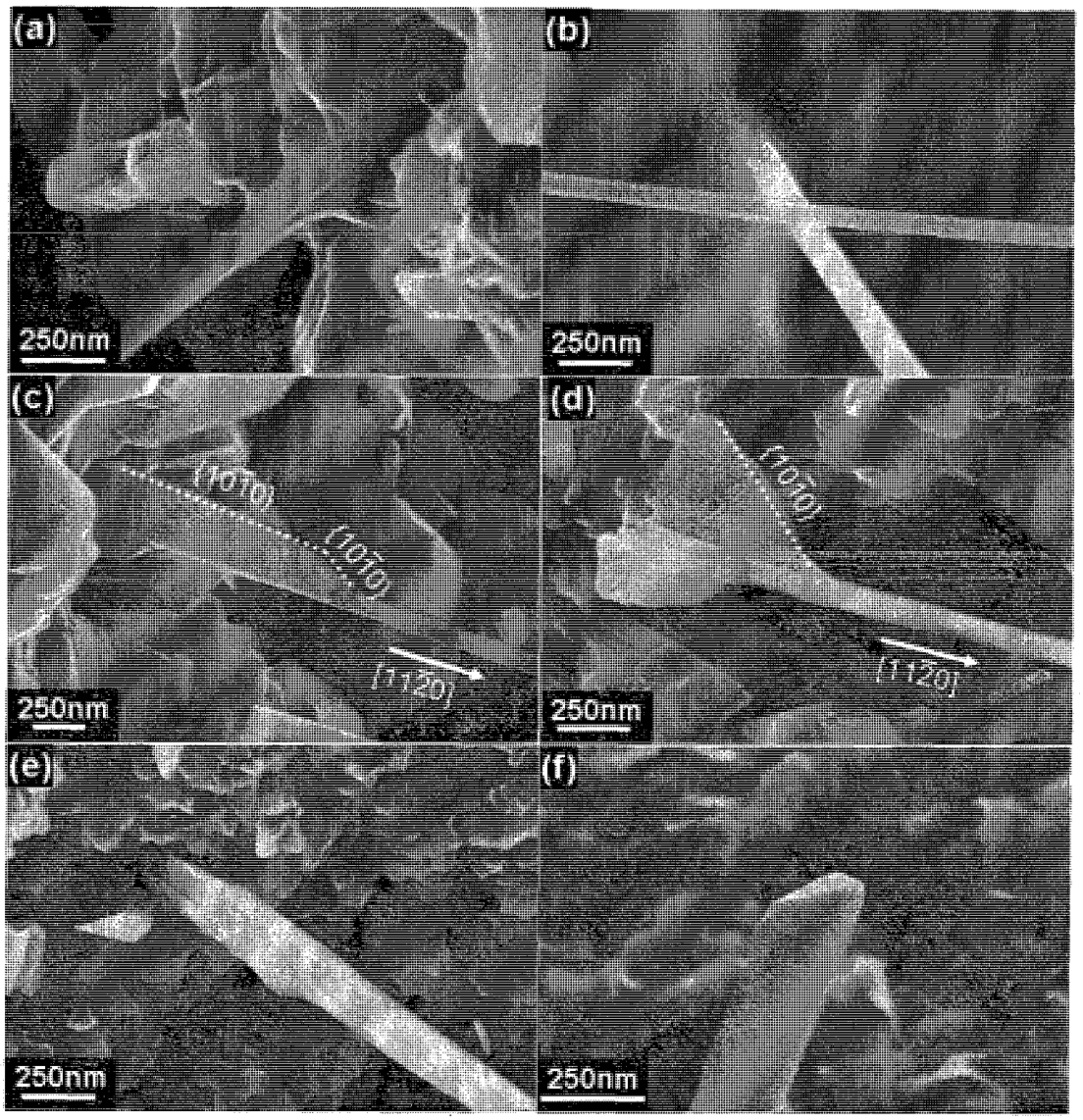

Figure 4.13: SEM images of nanowire nucleation sites and tips. (a) and (b) 850°C growth of two different nanowires. (a) Nucleation site. (b) NW tip. (c) Nucleation site of a 950°C nanowire. (d) Nucleation site of a 1000°C nanowire grown from the Type 2 matrix. (e) and (f) Two different nanowires from the Type 3 matrix of the 1000°C growth. (e) Nucleation site. (f) NW tip.

wurtzite and zinc-blende domains were observed in the nanowire, and the boundaries between the domains are marked in Figure 4.14. FFTs from each domain are given on the left side of the figure, and domains 1-4 were indexed as wurtzite with a $\langle 11\bar{2}0 \rangle$ zone axis while domain 5 was indexed as zinc-blende with a $\langle 011 \rangle$ zone axis. The arrows indicate the $\langle 0001 \rangle$ or $\langle 111 \rangle$ direction. The zinc-blende $\{111\}$ plane is equivalent to the wurtzite $\{0001\}$ plane, so the two crystalline phases can form a coherent interface along those planes. The arrows from domains 4 (wurtzite) and 5 (zinc-blende) are parallel, and the two domains share a long coherent interface, indicated by a solid line in Figure 4.14a. Domain 2 has additional crystal structure shown in Figure 4.14b. While the interfaces between wurtzite domains were incoherent, zinc-blende regions were able to fill in some of the gaps between the wurtzite domains with one or more coherent interfaces.

Domains 1, 3, and 4 all have two facets on $\{01\bar{1}1\}$ planes and one facet on the (0001) plane. For all three regions the (0001) facet is found at an internal interface, not on an external facet. The zinc-blende domain 5 faceted on the $\{111\}$ planes.

An analysis of the 950°C cross section is given here. In Figure 4.15a the nanowire is shown buried in gold and platinum to protect the wire from the ion beam. The cross section has an asymmetric shape and has a number of contrast features on it. These contrast features are related to the several crystallographic orientations within the nanowire. The boundaries between the crystalline domains are highlighted in Figure 4.15b. None of the domains are triangular in shape, while three of the four wurtzite domains from the 850°C cross section were triangular. FFTs for each domain are given on the right, and domains 2-4 were indexed as wurtzite with a $\langle 11\bar{2}0 \rangle$ zone axis while domain 1 was indexed as zinc-blende with a $\langle 011 \rangle$ zone axis. The arrows on the FFTs point toward the zinc-blende $\langle 111 \rangle$ or wurtzite $\langle 0001 \rangle$ directions. Three of the five wurtzite domains have similar orientations and are labeled 3a, 3b, and 3c to clarify their relation.

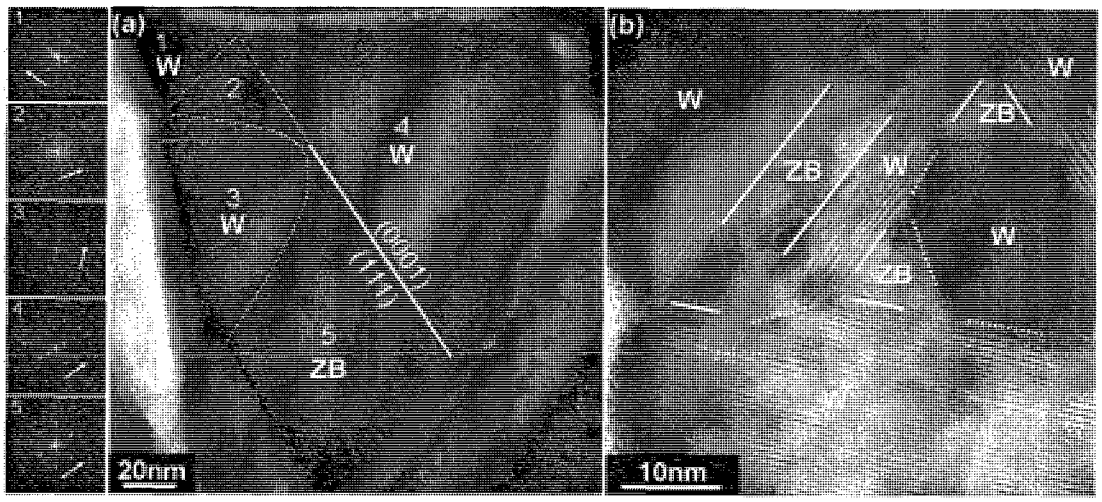

Figure 4.14: (a) Cross section of a nanowire grown at 850°C. Dotted lines indicate incoherent interfaces between crystal domains and solid lines indicate a coherent interface. FFTs for each domain is given on the left. (b) Close up of crystal domain 2. (Figure adapted from pictures published in Nanotechnology [7].)

A close-up of the central region of the nanowire, which includes the parallelogram-shaped zinc-blende region, is shown in Figure 4.15c. The zinc-blende domain is faceted on the {111} planes. The triangular light contrast region on the right hand side of the zinc-blende region appears to be amorphous. On the left side of the zinc-blende domain, a coherent interface is formed with the wurtzite (0001) plane of domain 2. This is confirmed in the FFTs of the two domains because the arrows pointing to the ⟨111⟩ and ⟨0001⟩ directions are parallel. The interfaces between the zinc-blende domain 1 and the wurtzite domains 3b and 3c (shown by the upper two dash-dot lines) are close to aligning. However, the orientations indicated in the FFTs are not perfectly aligned. Because the coherent planes are not perfectly aligned, stacking faults are expected and were observed. In the interface between domains 1 and 3c, the stacking faults last for about 20nm and the lower boundary to the stacking faults is indicated with the lowest dash-dot line. This region is neither zinc-blende or wurtzite, as confirmed by FFT. Along the wurtzite (0001) and zinc-blende (111) directions, the

only difference between the crystal structure is that wurtzite has ABAB stacking and zinc-blende has ABCABC stacking, so it is easy for planes of atoms to switch between the stacking orders.

Some of the interfaces between the wurtzite domains are shared by equivalent planes. The interface between between domain 2 and domain 3a are $\{0\bar{1}11\}$ planes. The interface between between domain 2 and domain 3c are $\{0\bar{1}13\}$ planes. The interface between between domain 3a and domain 3b are $\{0\bar{1}10\}$ planes. The equivalent planes in the interface between domains 2 and 3c and the interface between domains 3a and 3b are not aligned perfectly, causing thin regions of disorder at the interfaces.

The interfaces adjacent to domain 4 are not made up of equivalent planes. Zinc-blende/wurtzite stacking faults extend along the entire length of the interface between domains 3b and 4 and along about half of the interface between domains 3c and 4. The 3c/4 interface has a $\{0\bar{1}11\}$ plane on the 3c side that meets with a $\{0001\}$ plane from the domain 4 side. If domain 4 were directly adjacent to domain 1, the $\{0001\}$ wurtzite plane would be against the $\{010\}$ zinc-blende plane, which do not form a coherent interface. Considering that the crystalline orientation of domain 4 is so different from orientations of the adjacent domains, it is not surprising that the light contrast area between domains 1 and 4 is amorphous.

Domain 3b of the 950°C growth is the only wurtzite domain that has an external facet along the (0001) plane. All other wurtzite domains have external facets along the $\{0\bar{1}1x\}$ pyramid planes (see Figure 4.16).

4.2.3 Asymmetric Cross Sections

While some nanowires appeared to have symmetric triangular cross-sections, others did not. Nanowires with asymmetric cross sections were observed at all three growth temperatures (see Figure 4.17). End on views of these nanowires suggest multiple crystalline domains and the domains often have a triangular cross section. In SEM

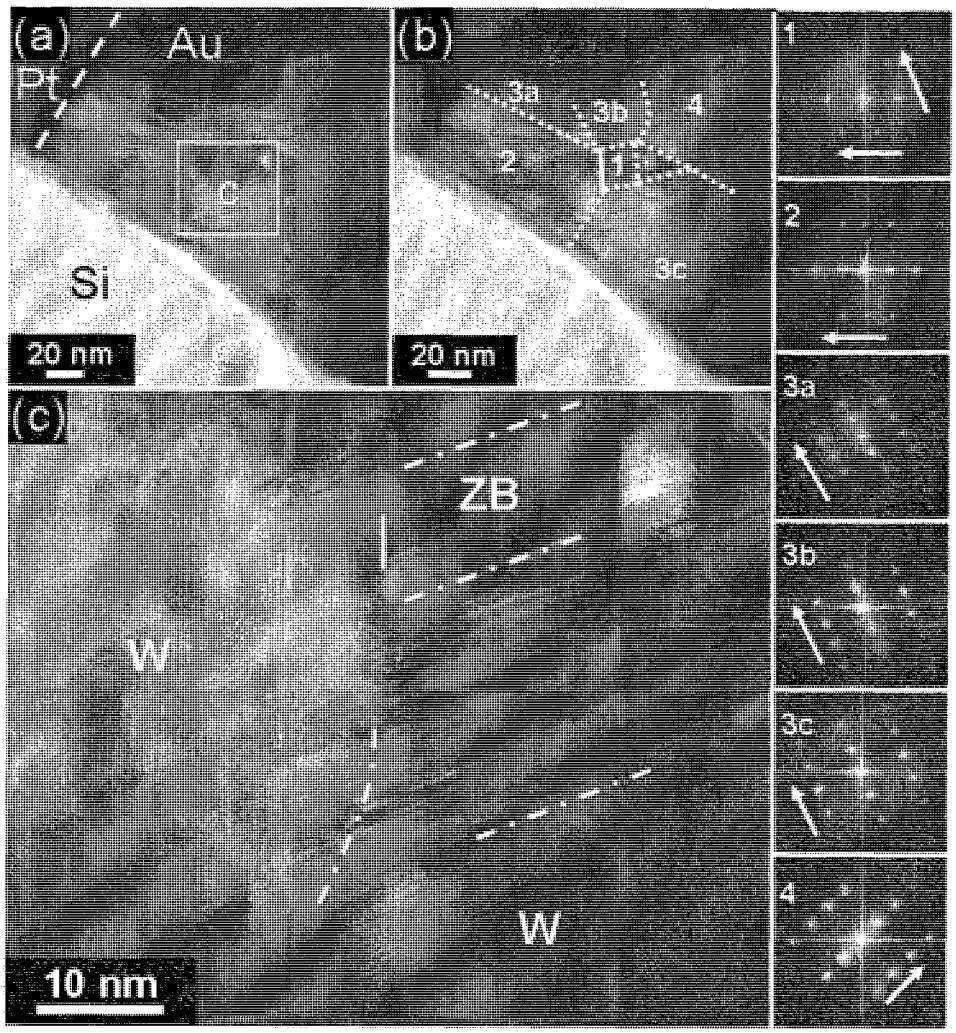

Figure 4.15: (a) Cross section of a nanowire grown at 950°C. The Au and Pt coatings protect the nanowire during the FIB process. (b) Outlines of the apparent crystallographic regions. FFTs of each region are given on the right. Region 1 was the only zinc-blende region; all other regions are various orientations of wurtzite GaN. Arrows on the FFTs point in the ⟨111⟩ direction for region 1 and in the ⟨0001⟩ direction for the others. (c) HRTEM of the interfaces between the zinc-blende and wurtzite regions. The solid line indicates a coherent interface the dash-dot lines indicate boundaries with stacking faults, and the curved dash-dot line indicates the boundary between domains 2 and 3c where equivalent planes nearly line up. (TEM images courtesy of B. W. Jacobs.)

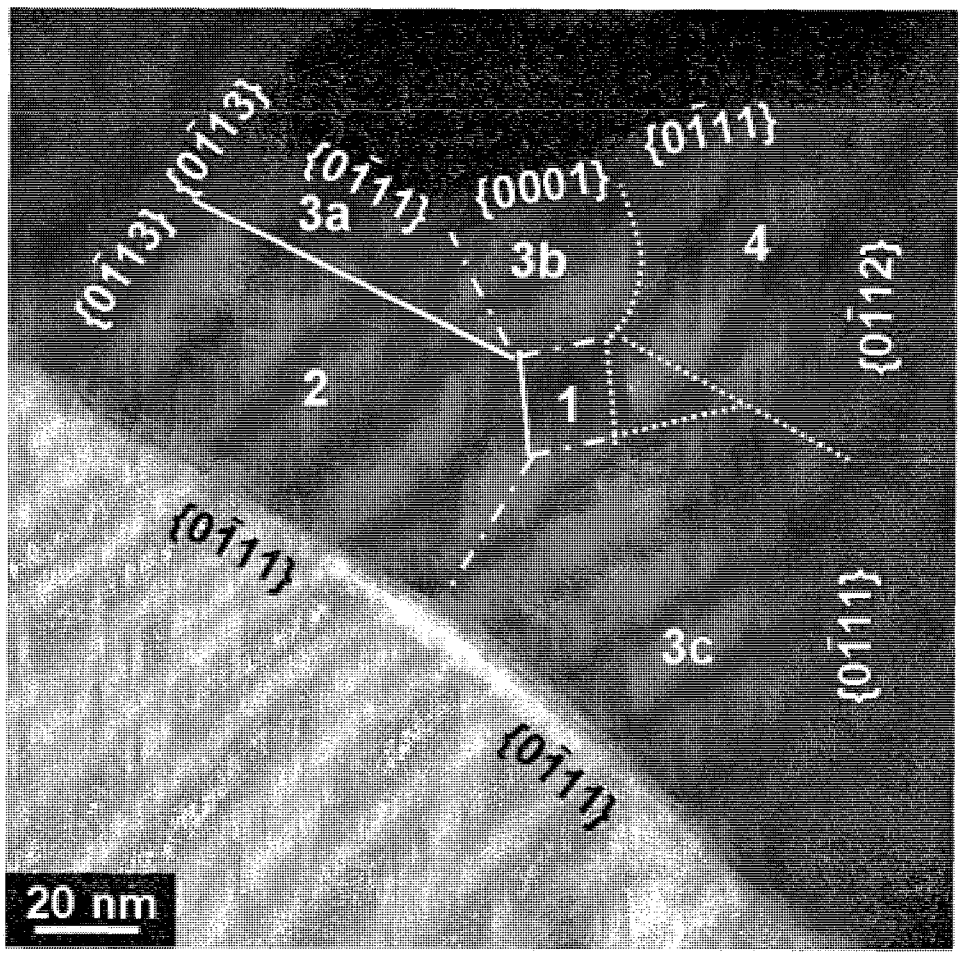

Figure 4.16: Side facets of the 950°C TEM cross section. The solid lines indicate coherent interfaces, dotted lines indicate incoherent interfaces, and dash-dot lines indicate equivalent planes that nearly line up. (TEM image courtesy of B. W. Jacobs.)

images of the 850°C and 950°C growths, nanowires that had non-symmetric cross sections were generally shorter than other nanowires in the growth, suggesting that the non-symmetric nanowires grew at a slower rate. The apparent domains are comparable in size to the domains observed in the TEM cross sections. Like the TEM cross section of the nanowire grown at 950°C, these nanowires are likely to be shaped this way in order to accommodate stacking faults between different crystal domains.

4.3 [0001] Nanowire and Rod Nucleation and Growth

This section deals with nanowires and rods that grow in the ⟨0001⟩ direction and are typically single phase with a hexagonal cross section 0.1-30 μm in width.

4.3.1 SEM of [0001] Nanowires and Rods

Rods have a [0001] growth direction, hexagonal cross sections, and were observed only in the Type 1 regions of the 1000°C growth. SEM images showing the connection of the base of the rod to the matrix are shown in Figure 4.18 and confirm the [0001] growth direction. Most, but not all, rods taper near the tip region, which has different facets than the rest of the rod. SEM images of the tips of the rods are shown in Figure 4.19. The tip shown in Figure 4.19a appears to have a spiral. In Figure 4.19b the rod has a hole off-set from the center of the rod. The hole was deep enough that any feature at the bottom was not able to be observed because the electrons could not escape the hole. In both Figure 4.19a and b the faceting of the tip are the $(11\bar{2}1)$ pyramid planes of the a face. Both the spiral shape of a tip and the presence of a small deep hole in a rod are indicators of a screw dislocation growth mechanism. Figure 4.19c shows a side view of a different rod tip.

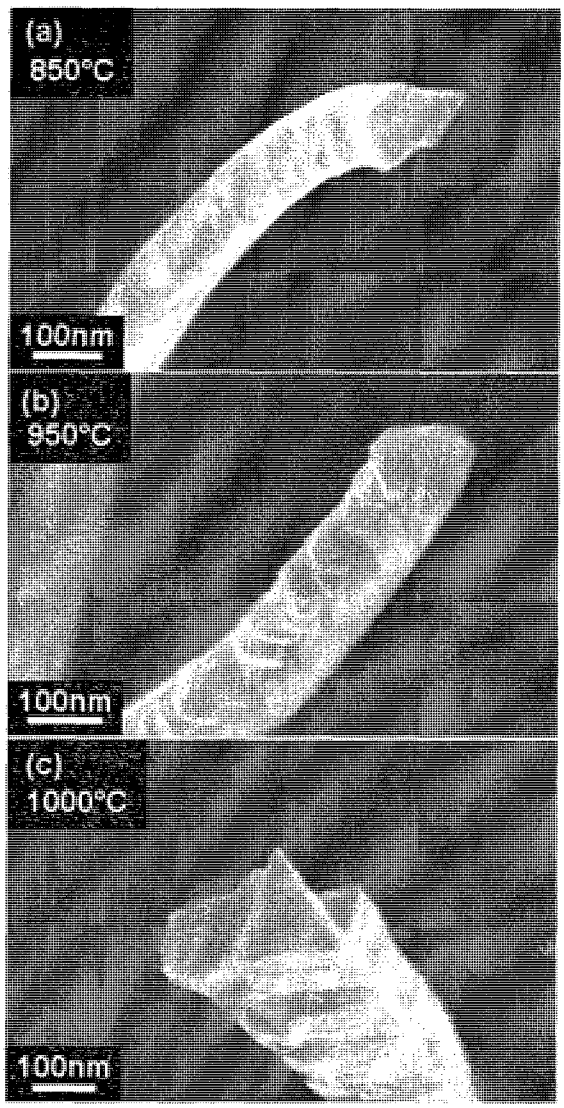

Figure 4.17: Non-symmetric nanowires were observed at each growth temperature. The nanowire shown for the 1000°C growth originated from the Type 2 matrix area, which is the matrix type most similar to the matrix observed at 850°C and 950°C.

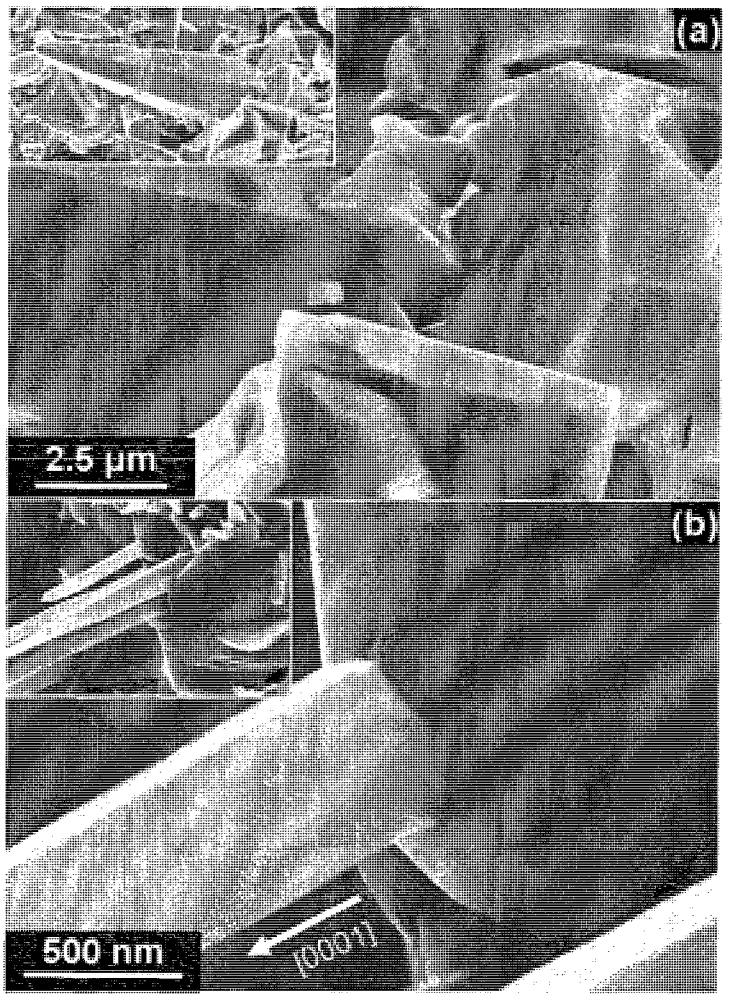

Figure 4.18: (a) Rod base from step-ledge c-face. (b) Rod base from $10\bar{1}1$ planes.

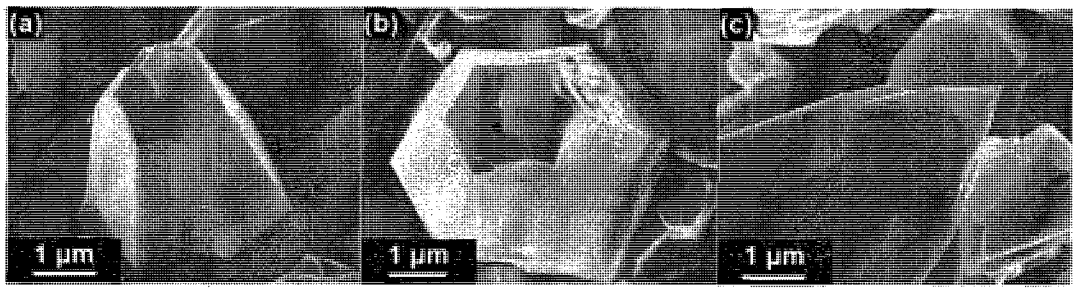

Figure 4.19: (a) Rod end displaying spiral growth. (b) Rod imaged end on with a hole off the center of the rod. (c) View of a rod from the side showing the pointed end structure.

4.3.2 TEM Nanowire Cross Sections: Nanowires as a Nucleation Mechanism Diagnostic

A cross section of a cluster of rods and nanowires grown at 1000°C is shown in Figure 4.20a. Three of the four rods and one of the two nanowires had a light contrast area near the center of the rod or nanowire [8]. A close up of one of the rods and its light contrast area is shown in Figure 4.20b. The light contrast area appears to be completely electron transparent, indicative of a nanopipe in the center of this rod.

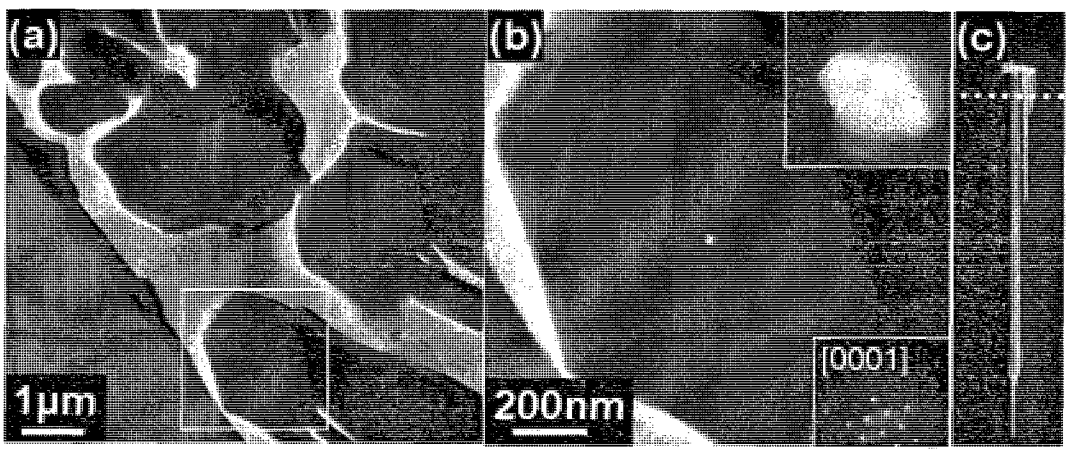

Figure 4.20: (a) Cross section of a cluster of rods grown at 1000°C. (b) Close-up of the bottom rod in (a). Insets show that the rod is oriented along the [0001] zone axis and that the light contrast area near the center of the rod appears to be electron transparent. (c) SEM of the cluster of rods. The dotted line indicates where the cross section was made near the base of the rods. (Figure adapted from pictures published in Nano Letters [8])

Chapter 5

Models of Crystal Formation

Crystals grow due to supersaturation of the vapor surrounding the crystal. The level of supersaturation is one parameter that can effect crystal morphology. Evidence of local supersaturation effecting crystal growth is presented in the first section. Relaxation also plays a role in determining the final crystal morphology. Relaxation is first discussed in the matrix growth in the context of growth twins. Relaxation mechanisms are then discussed in the $\langle 0001 \rangle$ rod growth and finally in the $\langle 11\bar{2}0 \rangle$ nanowire growths.

5.1 Supersaturation

Crystal morphology is inherently tied to the conditions in which the crystals were formed. Crystal growth requires a supersaturation of the constituent atoms in the liquid or vapor surrounding the crystal, otherwise the crystal would lose atoms or remain at equilibrium with its environment. However, crystal growth mechanisms are a function of the level of supersaturation. This is illustrated in Figure 5.1. An adatom is more likely to stay on the surface if it can bond to more than one atom in the crystal lattice. At low supersaturations, the density of adatoms is low, so atoms

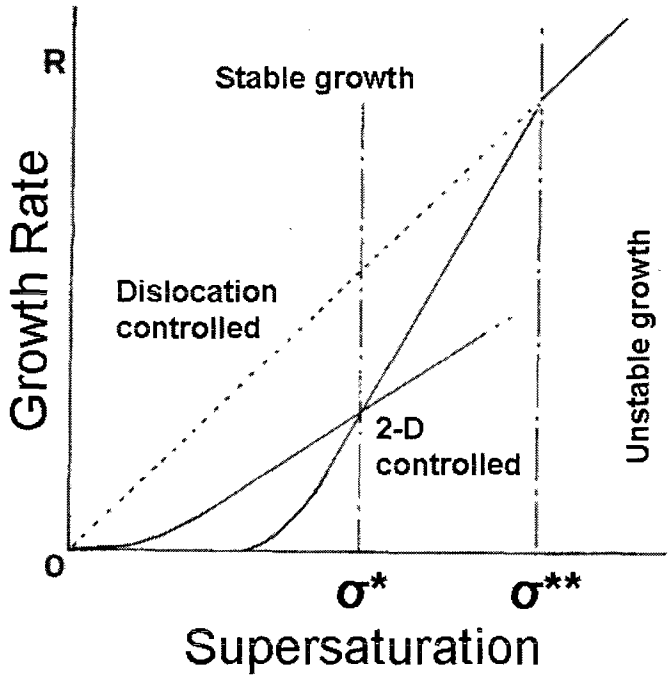

Figure 5.1: Growth rate as a function of supersaturation. (Image from Wilcox [9]).

will tend to stay on the surface only if they find a ledge or a kink in the surface. Ledges and kinks are caused by dislocations in the crystal, and at low supersaturations crystal growth is predominantly caused by dislocations. At higher supersaturations, adatoms aggregate together until they form a cluster large enough that it is unlikely for the atoms to remove themselves from the surface. This is known as 2D nucleation. At very high supersaturations, adatoms can easily stick to the surface of the crystal, even surfaces with higher surface energies, which causes branching. A structure with repeated branching is known as a dendrite. There is evidence for all three of these growth mechanisms in the 1000°C growth.

5.1.1 Dislocation Driven Growth

The nanopipes that were observed in the rods by both SEM and TEM cross section (Figures 4.19b and 4.20) are compatible with a screw dislocation growth mechanism and may represent dislocation driven growth.

5.1.2 2D Growth

Layered formations were commonly observed on the c faces of the Type 1 matrix in the 1000°C growth (Figure 5.2a-c). These layers do not show evidence of spiral patterns that would indicate a screw dislocation. The layers are tens of nanometers thick, so each observed layer is composed of several layers of atoms. Similar layers were observed in the cross section of the 850°C matrix (Figure 5.2d).

5.1.3 Dendrites

Dendritic growth was observed near the base of a group of rods (see Figure 5.3). This group of rods is similar to the group of rods shown in Figure 4.20c used for the TEM cross section and it is reasonable to assume that they too grew from a screw dislocation growth mechanism. Because the dendritic growth was so close to the rod growth, considerable variation of the local supersaturation is likely.

5.2 Crystallography of the Matrix: Twinning

The crystal formations on the surface of the matrix changed considerably from 850°C to 1000°C. This section describes various crystal morphologies and how they relate to the crystal structure.

In this growth process, the polycrystalline matrix exhibits several morphologies. Some of the more exotic crystal morphologies provide evidence for twinning. Twins

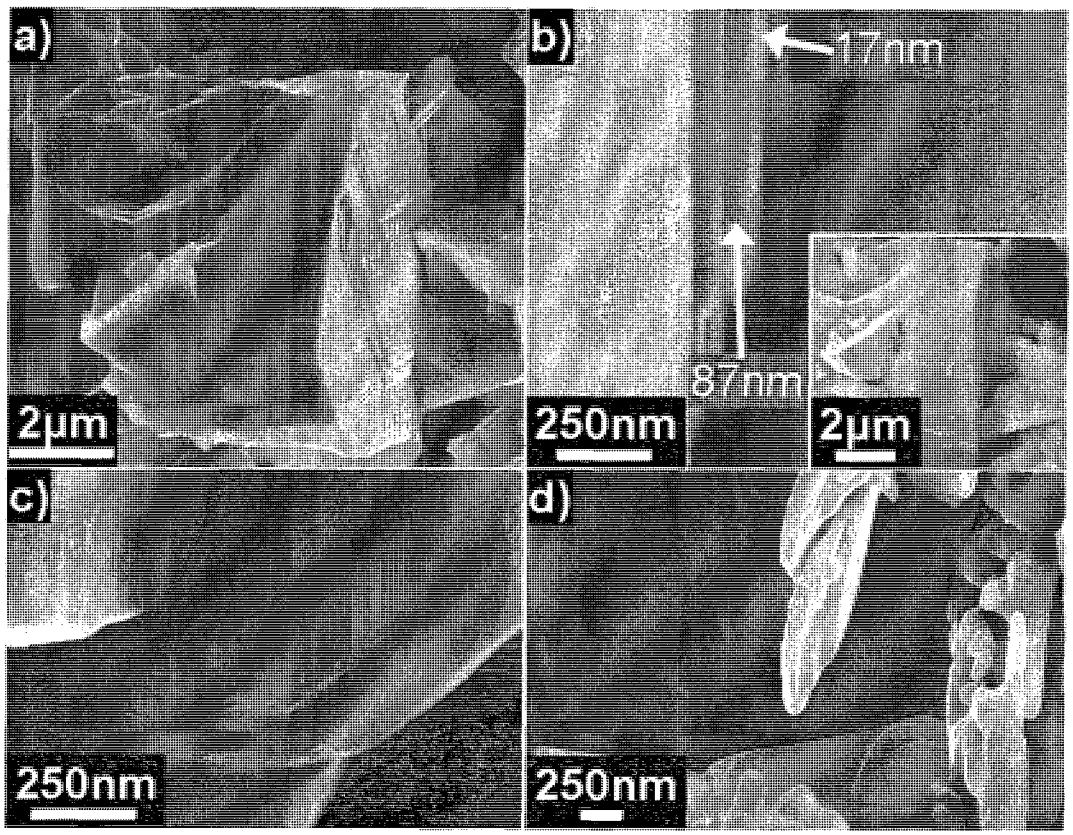

Figure 5.2: (a) Layered growth of the matrix at 1000°C. (b) Matrix from (a) tilted for a side view. (c) Layered growth at 1000°C making pyramid planes. (d) Layers observed in the 850°C matrix cross section.

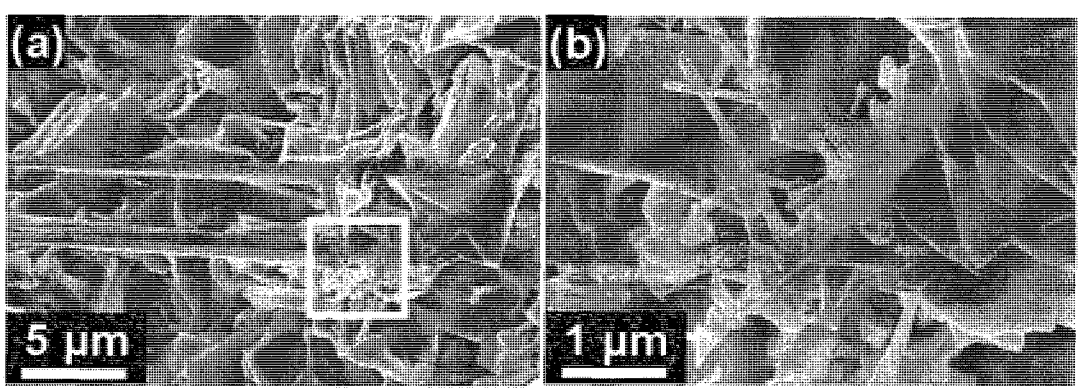

Figure 5.3: (a) Rods from parallel growth at 1000°C. Near the base of the rods is some dendritic growth. (b) Close up of the dendritic growth.

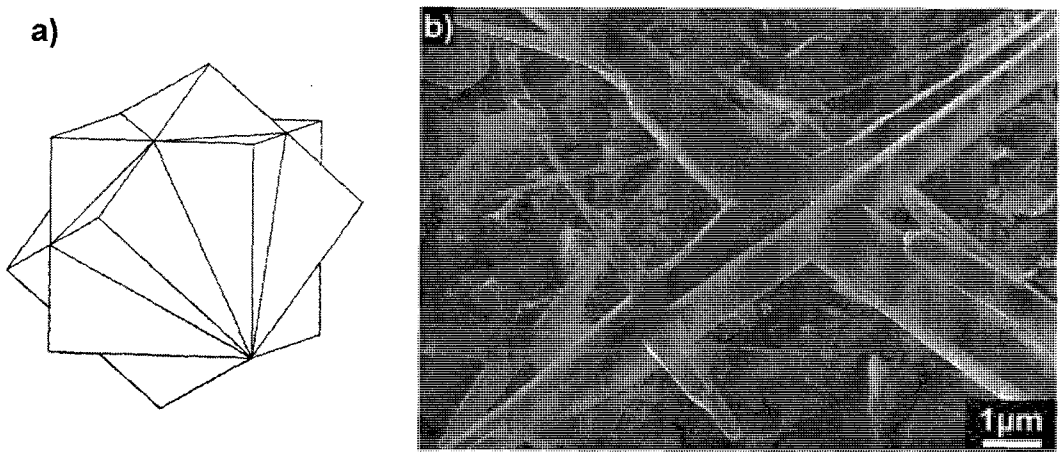

Figure 5.4: (a) Interpenetrant cubes twinned about a triad axis [10]. (b) Growth at 950°C.

can arise from the growth process, from a transformation as the system cools down from growth, or as a result of stress after the crystal has formed [65]. Comparisons between SEM images and various models of crystal twinning and morphology given in Phillips [10] and Hahn [11] are illustrated in Figures 5.4, 5.5, 5.6, and 5.7. While none of these features were common in these samples, each type of feature was observed in at least two instances in the temperature series samples.

The first type of twinning is known as an *interpenetrant twin.* In these cases, there is no well-defined plane of crystal orientations, but the two orientations seem to grow through each other. In the temperature series, this type of twinning was only observed in nanowires grown at 950°C where two wires intersected and seemed to grow through each other (Figure 5.4).

The most frequently observed twinning was along the c direction in the matrix in the 1000°C growth. Figure 5.5a shows a twinned octahedron. An octahedron has the same symmetry as a cube, and the faces of an octahedron correspond to the {111} face of a cube. Because a cubic {111} face is equivalent to the hexagonal {0001} face, the twinned octahedron can represent twinning perpendicular to the c direction of

wurtzite. This is further exemplified in the hexagonal symmetry of the twin plane shown in Figure 5.5b.

The next type of twinning is the elbow (or geniculate) twin. Figure 5.6a shows a schematic of a tetragonal elbow twin and b) and c) show multiple elbow twins. A similar type of morphology has been observed at 1000°C.

Parallel-growth, while not a form of crystal twinning, also involves adjacent crystals with the same, or nearly the same, orientation of all edges. At 1000°C, two different types of parallel-growth were observed. The first type is when the width of the wire varies along the length of the wire, as shown in Figure 5.7b. The second type is where multiple structures are connected at the base by a single structure, as shown in Figure 5.7c.

Except for the interpenetrant twinning, which occurred in the 950°C growth, twinning was generally observed in the Type 1 matrix growth at 1000°C. None of these morphologies were observed in the 850°C growth. The surface of the Type 1 matrix has more distinct faceting, which may allow the twins to be recognized more easily. It could be that the larger size of the crystalline platelets are formed by growth processes similar to macroscopic crystals. Additionally, the larger crystal size and distinct faceting may make each platelet less accommodating of strain at the crystal interfaces, resulting in twinning to reduce strain.

5.3 Nanowire and Rod Growth

5.3.1 Discussion of the [0001] Growth Direction Nucleation Mechanism

Nanopipes have been observed both at the tip of a rod (Figure 4.19b) and near the base of rods (Figure 4.20c). The nanopipes observed in these rods and nanowires

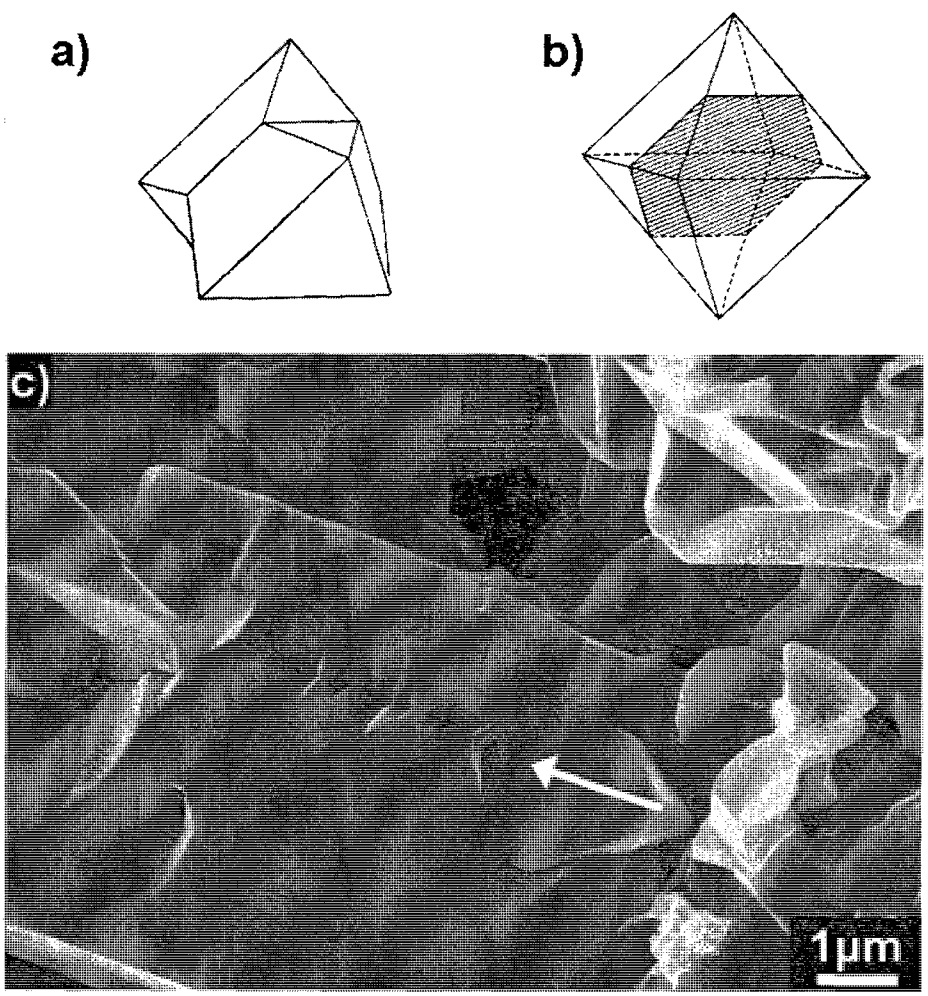

Figure 5.5: (a) A twinned octahedron [10]. (b) The twin plane of (a) [10]. (c) Growth at 1000°C. The arrow is parallel with the twin plane. (Image courtesy of B. W. Jacobs.)

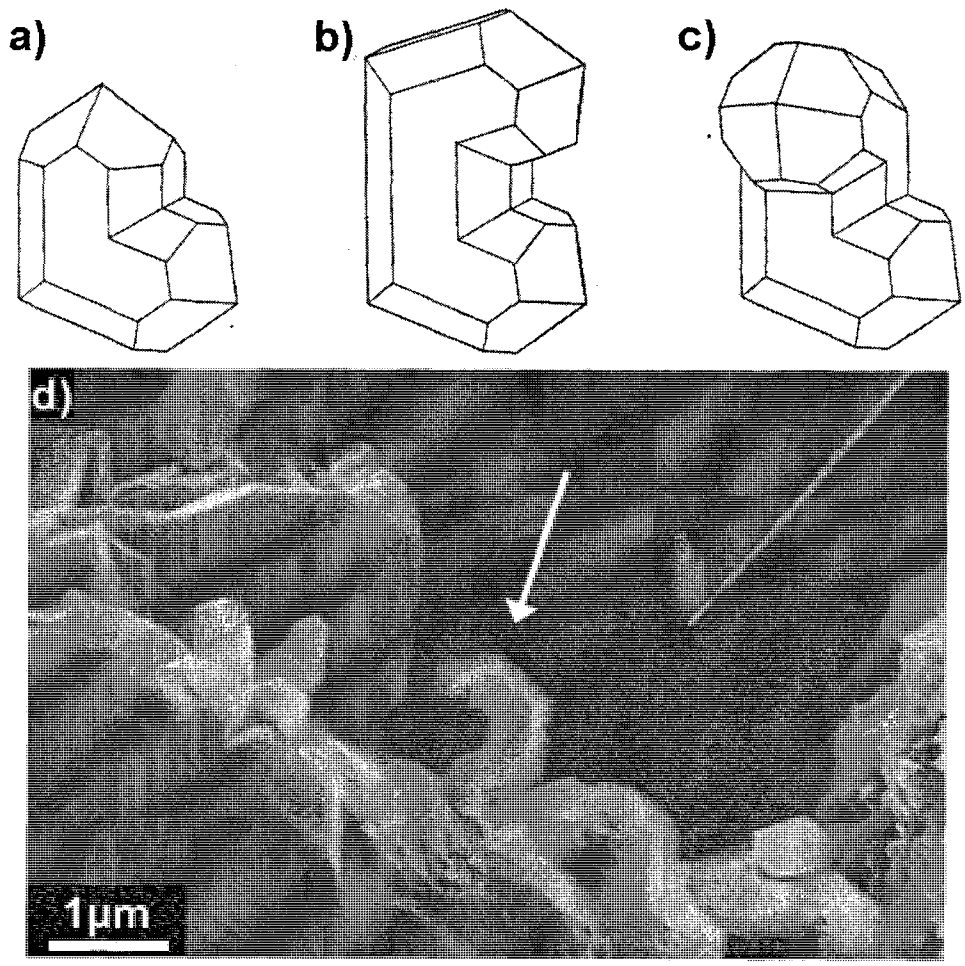

Figure 5.6: (a) Elbow twin of a tetragonal crystal [10]. (b) and (c) Repeated elbow twinning [10]. (d) Growth at 1000°C.

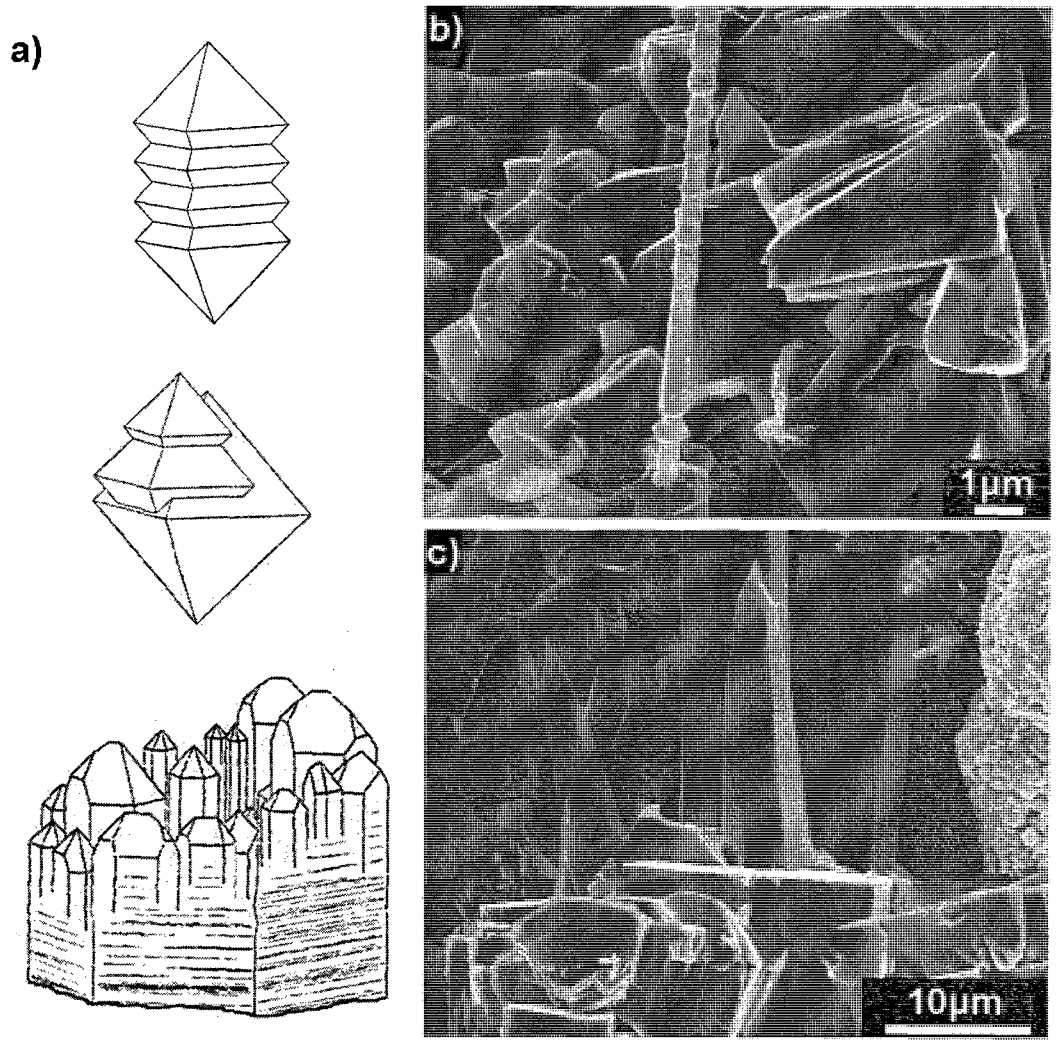

Figure 5.7: (a) top and middle: Parallel growth of octahedra [10]. bottom: Parallel growth of hexagonal prisms [11]. (b) Rod growth at 1000°C. (Image courtesy of B. W. Jacobs.) (c) Growth at 1000°C.

indicate that a screw dislocation growth mechanism is likely. Although the screw dislocation is what allows the rod to grow, it also introduces strain immediately surrounding the dislocation. If the Burger's vector of a screw dislocation is large, a hollow core will form in order to relieve strain from the dislocation. At this point, it is more energetically favorable for the system to accommodate the surface energy of the sides of the nanopipes than to have an enormous strain around the dislocation.

5.3.2 Discussion of the $\langle 11\bar{2}0 \rangle$ Growth Direction Nucleation Mechanism

The change in growth direction from $\langle 11\bar{2}0 \rangle$ to [0001] was caused by a change in the matrix from which the nanowires and rods nucleate. At the lower temperatures and in the Type 2 and 3 matrix regions of the 1000°C growth, nanowires nucleate from the nanoscale ledges of the platelets, whereas in the Type 1 matrix, rods form from screw dislocations. It is possible that exposed $\{11\bar{2}0\}$ planes of multiple nanoscale ledges (see Figure 4.12) act as nucleation sites to the wurtzite domains of the nanowires. Both the nanoscale ledges and the individual crystal domains observed in the TEM cross sections of the nanowires are on the order of tens of nanometers wide. Any zinc-blende component of the nanowires may form in order to relieve strain between the multiple wurtzite domains. We have not found evidence of a zinc-blende nucleation site in the matrix, so it is likely that the zinc-blende forms as a relaxation mechanism to relieve strain between the multiple wurtzite domains of the nanowire. All the zinc-blende regions found in the 850°C and 950°C cross sections had at least one coherent interface with a wurtzite region. This suggests that the zinc-blende regions could originate from one of the wurtzite regions, just by changing the stacking order from ABAB to ABCABC in order to accommodate strain on the other sides.

This proposed growth mechanism is a new variation of templated nanowire growth.

Wurtzite domains provide a self-assembled template whereby a zinc-blende nanowire forms in order to relieve strain between the wurtzite domains.

Chapter 6

Conclusions

Matrix growth surface morphology is dependent on the temperature, however, at all three temperatures studied, the matrix platelets were found to be wurtzite by XRD. In the 1000°C growth, multiple types of twinning was observed in the matrix with the largest platelet formations.

One advantage of catalyst free nanowire growth is that the growth mechanism is not limited by the catalyst. This study identifies three different nanowire growth mechanisms that occurred in our samples of catalyst free GaN nanowire growth: multidomain nanowire growth in the $\langle 011 \rangle / \langle 11\bar{2}0 \rangle$ directions from nanoscale ledges at the edge of wurtzite platelets, hexagonal rod growth in the $\langle 0001 \rangle$ direction from screw dislocations, and dendritic nanowire growth due to a high local supersaturation.

Nanowires with multiple crystalline domains can have very complex structures. These nanowires may have triangular cross sections or they may have asymmetric cross sections with triangular components. The crystalline domains try to align to other domains by matching equivalent planes, but this is not always possible. In order to relieve internal strain, zinc-blende domains are formed by changing the stacking order of the c-face planes, creating a zinc-blende nanowire within the wurtzite domains. This represents a novel method of templated nanowire growth.

Hexagonal rods form from screw dislocations and are associated with regions that may have had a low local supersaturation during growth. These rods sometimes exhibit holes, which indicate that the Burger's vector of the dislocation is very large. Dendritic nanowires could be found originating from matrix close to the rods and possibly formed due to high local supersaturation.

Future work on this nanowire growth could include using a nanomanipulator to select a nanowire-platelet pair to prepare a sample for TEM. To date, a nanowire connected to a growth matrix platelet has not been observed in the TEM. This would give more information about the interface between the nanowire and the platelet, as well as allow for observation of the platelet edges to test our hypothesis that nanowires nucleate from nanoscale ledges of the platelets.

Another interesting experiment would be an attempt to synthesize rough platelet edges to control nanowire growth locations and internal structure. Such experiments would give further insight to multiphase nanowire formation and allow for closely controlled experiments on electronic properties of these nanowires. Multiphase nanowires will have unique electronic characteristics because crystal structure is inherently tied to the electronic properties of a material.

The results from this thesis give further insight into the methods and mechanisms of nanowire growth in a catalyst free environment. Fundamental understanding of nanowire growth will aid future development of applications and devices utilizing nanowires.

Appendix A

Appendix: Structure Factor Calculations for Zinc-Blende and Wurtzite GaN

The structure factor is given by

$$F = \sum_j f_j e^{-i\hat{K}\cdot\hat{r}_j} \tag{A.1}$$

where f_j is the atomic form factor, $\hat{K}$ is the reciprocal lattice vector, and $\hat{r}_j$ is the position vector of the atom. The sum is over all atoms of the unit cell.

For GaN, the atomic form factor f_j will be different for Ga and N and the values can be looked up in the International Tables for Crystallography [66]. However, because my main purpose in calculating the structure factor is to determine which Bragg reflections are allowed ($F \neq 0$) and which are not ($F = 0$), it will be assumed that the Ga and N portions of the structure factor do not perfectly cancel each other out. This is a reasonable assumption, as will be shown later on.

A.1 Zinc-blende Structure Factor

Consider the zinc-blende structure to be the simple cubic structure with a basis of 8 atoms. The position of each atom is given by

$$\begin{aligned}
\hat{r}_1 &= 0 \\
\hat{r}_2 &= \frac{a}{2}(\hat{x}+\hat{y}) \\
\hat{r}_3 &= \frac{a}{2}(\hat{x}+\hat{z}) \\
\hat{r}_4 &= \frac{a}{2}(\hat{y}+\hat{z}) \\
\hat{r}_5 &= \frac{a}{4}(\hat{x}+\hat{y}+\hat{z}) \\
\hat{r}_6 &= \frac{3a}{4}(\hat{x}+\hat{y})+\frac{a}{4}\hat{z} \\
\hat{r}_7 &= \frac{3a}{4}(\hat{x}+\hat{z})+\frac{a}{4}\hat{y} \\
\hat{r}_8 &= \frac{3a}{4}(\hat{y}+\hat{z})+\frac{a}{4}\hat{x}
\end{aligned} \tag{A.2}$$

and can be visualized in Figure A.1.

The reciprocal lattice vector of a simple cube is

$$\hat{K} = \frac{2\pi}{a}(h\hat{x}+k\hat{y}+l\hat{z}) \tag{A.3}$$

Substituting equations A.2 and A.3 into equation A.1 and arbitrarily choosing Ga to be in the $\hat{r}_1$ position, the structure factor is

$$\begin{aligned}
F &= f_{Ga}[e^{-i\pi(0)}+e^{-i\pi(h+k)}+e^{-i\pi(h+l)}+e^{-i\pi(k+l)}]+ \\
&\quad f_N[e^{-i\pi/2(h+k+l)}+e^{-i\pi/2(3h+3k+l)}+ \\
&\quad e^{-i\pi/2(3h+k+3l)}+e^{-i\pi/2(h+3k+3l)}]
\end{aligned} \tag{A.4}$$

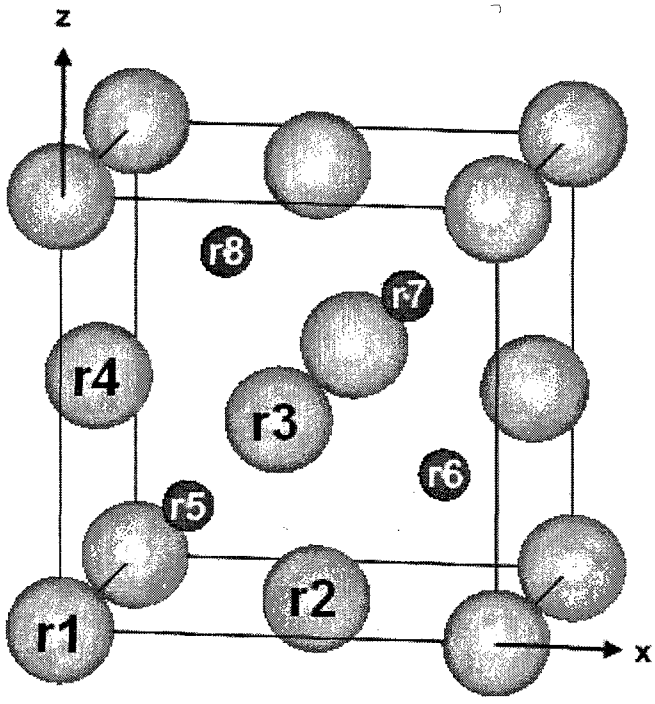

Figure A.1: Illustration of the position of each atom in the basis of the zinc-blende structure. (Image produced using the VESTA software package [4].)

h	k	l	Ga Atoms	N Atoms	Structure Factor
0	0	1	0	0	0
0	1	1	0	0	0
1	1	1	4	$4i$	$4f_{Ga}$+$4if_N$
0	0	2	4	-4	$4f_{Ga}$-$4f_N$
0	1	2	0	0	0
1	1	2	0	0	0
0	2	2	4	4	$4f_{Ga}$+$4f_N$
0	0	3	0	0	0
1	2	2	0	0	0
0	1	3	0	0	0
1	1	3	4	$-4i$	$4f_{Ga}$-$4if_N$
2	2	2	4	-4	$4f_{Ga}$-$4f_N$
0	2	3	0	0	0
1	2	3	0	0	0
0	0	4	4	4	$4f_{Ga}$+$4f_N$
0	1	4	0	0	0
2	2	3	0	0	0

Table A.1: Results of the zinc-blende structure factor calculations.

Since $e^{-i\pi} = -1$ and $e^{-i\pi/2} = -i$, equation A.4 simplifies to

$$\begin{aligned} F &= f_{Ga}[1 + (-1)^{h+k} + (-1)^{h+l} + (-1)^{k+l}] + \\ &\quad f_N[(-i)^{h+k+l} + (-i)^{3h+3k+l} + \\ &\quad (-i)^{3h+k+3l} + (-i)^{h+3k+3l}] \end{aligned} \tag{A.5}$$

The structure factor was calculated for all planes that could diffract with $2\theta \leq 90°$. As shown in Table A.1, all but six of the planes have a structure factor of zero, meaning only six intensity peaks would be observed in the range $2\theta \leq 90°$. The intensity of diffraction is proportional to $|F|^2$, so complex structure factors are not a problem. Because the masses of gallium and nitrogen are so different, the atomic scattering factors f_{Ga} and f_N are also quite different, as can be verified in the International Tables for Crystallography [66]. Thus structure factors such as $4f_{Ga}$-$4f_N$ will not be zero.

A.2 Wurtzite Structure Factor

For wurtzite GaN, finding the reciprocal lattice vector and the position of the atoms involves more geometry because the unit vectors are not perpendicular. Since wurtzite is the hcp structure with a two atom basis, and hcp is the simple hexagonal structure with a two atom basis, the reciprocal lattice vector of the simple hexagonal structure can be used. The unit vectors illustrated in Figure A.2 can be described mathematically by

$$\begin{aligned} \hat{a}_1 &= a\hat{x} \\ \hat{a}_2 &= \frac{a}{2}\hat{x} + \frac{a\sqrt{3}}{2}\hat{y} \\ \hat{a}_3 &= c\hat{z} \end{aligned} \tag{A.6}$$

The reciprocal lattice vectors are therefore

$$\begin{aligned} \hat{b}_1 &= 2\pi\frac{\hat{a}_2 \times \hat{a}_3}{\hat{a}_1 \cdot (\hat{a}_2 \times \hat{a}_3)} \\ &= \frac{2\pi}{a\sqrt{3}}(\sqrt{3}\hat{x} - \hat{y}) \\ \hat{b}_2 &= 2\pi\frac{\hat{a}_3 \times \hat{a}_1}{\hat{a}_2 \cdot (\hat{a}_3 \times \hat{a}_1)} \\ &= \frac{4\pi}{a\sqrt{3}}\hat{y} \\ \hat{b}_3 &= 2\pi\frac{\hat{a}_1 \times \hat{a}_2}{\hat{a}_3 \cdot (\hat{a}_1 \times \hat{a}_2)} \\ &= \frac{2\pi}{c}\hat{z} \end{aligned} \tag{A.7}$$

The reciprocal lattice vector $\hat{K}$ is therefore

$$\begin{aligned} \hat{K} &= h\hat{b}_1 + k\hat{b}_2 + l\hat{b}_3 \\ &= h\frac{2\pi}{a\sqrt{3}}(\sqrt{3}\hat{x} - \hat{y}) + k\frac{4\pi}{a\sqrt{3}}\hat{y} + l\frac{2\pi}{c}\hat{z} \end{aligned} \tag{A.8}$$

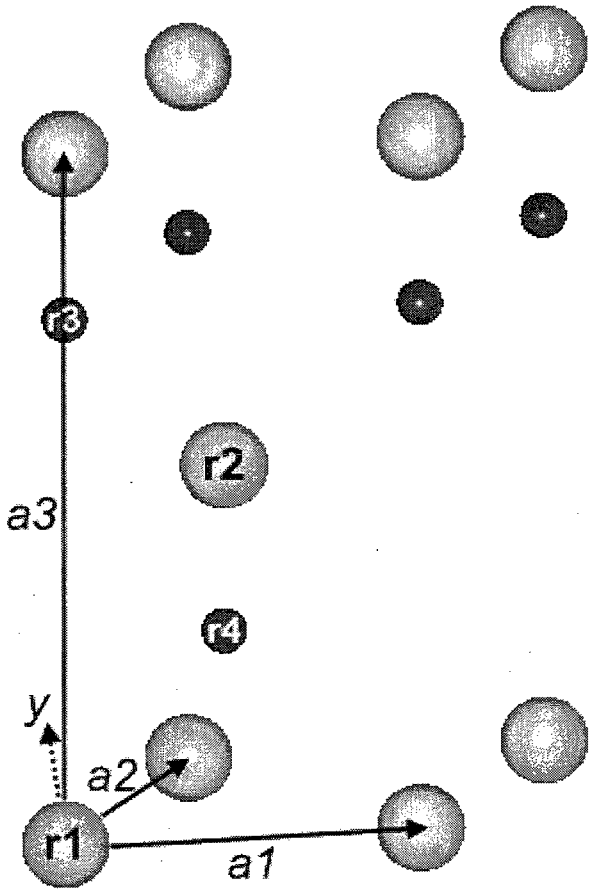

Figure A.2: Illustration of the coordinate system used in these calculations and the position of each atom in the basis of the wurtzite structure. $\hat{a}_1$ is in the $\hat{x}$ direction and $\hat{a}_3$ is in the $\hat{z}$ direction. (Image produced using the VESTA software package [4].)

The atomic positions for an hcp crystal would be

$$\begin{aligned} \hat{r}_1 &= 0 \\ \hat{r}_2 &= \frac{a}{2}\hat{x} + \frac{a}{2\sqrt{3}}\hat{y} + \frac{c}{2}\hat{z} \end{aligned} \tag{A.9}$$

For wurtzite we need to add two more atoms to the basis. In order to express the $\hat{z}$ components correctly, it is necessary to recognize that there are two different distances between the planes of gallium and nitrogen. One side of each plane is separated to the next by the bond length between a gallium atom and a nitrogen atom. The other side of each plane is separated by the height of the pyramid formed when one atom is directly above a triangle formed by three atoms of the opposite type. Because the base triangle has sides of equal length, the pyramid is a *regular triangular pyramid* which has the property that [67]

$$e = \sqrt{h^2 + \frac{a^2}{3}} \tag{A.10}$$

where e is the length of the edge of the pyramid, h is the height of the pyramid, and a is the length of the side of the base of the pyramid (i.e. it is the lattice constant a). However, Equation A.10 has two unknowns, e and h, but because e is equivalent to the bond length between a gallium atom and a nitrogen atom, we can relate these quantities to the lattice constant c:

$$\frac{c}{2} = h + e \tag{A.11}$$

Using Equations A.10 and A.11 to solve for h and e in terms of the lattice constants

a and c results in

$$\begin{aligned} h &= \frac{3c^2 - 4a^2}{12c} \\ e &= \frac{3c^2 + 4a^2}{12c} \end{aligned} \tag{A.12}$$

From this it can be determined that the other two atoms are at the points

$$\begin{aligned} \hat{r}_3 &= \left(c - \frac{3c^2 + 4a^2}{12c} \right) \hat{z} \\ \hat{r}_4 &= \frac{a}{2}\hat{x} + \frac{a}{2\sqrt{3}}\hat{y} + \frac{3c^2 - 4a^2}{12c}\hat{z} \end{aligned} \tag{A.13}$$

Using Equations A.8, A.9, and A.13 in equation A.1, the structure factor is

$$\begin{aligned} F &= f_{Ga}[e^{-i\hat{K}\cdot\hat{r}_1} + e^{-i\hat{K}\cdot\hat{r}_2}] + f_N[e^{-i\hat{K}\cdot\hat{r}_3} + e^{-i\hat{K}\cdot\hat{r}_4}] \\ &= f_{Ga}[1 + (-1)^{\frac{2}{3}h + \frac{2}{3}k + l}] + \\ &\quad f_N[(-1)^{(2 - \frac{3c^2+4a^2}{6c^2})l} + (-1)^{\frac{2}{3}h + \frac{2}{3}k + \frac{3c^2-4a^2}{6c^2}l}] \end{aligned} \tag{A.14}$$

When $\hat{r}_3$ or $\hat{r}_4$ is dotted with A.8, the values for the lattice constants will not cancel out, so it is necessary to know the numerical values for a and c. For GaN, they are [68]

$$\begin{aligned} a &= 3.19 \times 10^{-10} \\ c &= 5.18 \times 10^{-10} \end{aligned} \tag{A.15}$$

Table A.2 displays the calculated structure factor for all planes that could diffract with $2\theta \leq 90^\circ$. None of the planes results in a structure factor of zero, so a diffraction peak is expected to occur for each plane.

h	k	l	Ga Atoms	N Atoms	Structure Factor
1	0	0	0.5+0.9i	0.03+0.3i	(0.5+0.9i)f_{Ga}+(0.03+0.3i)f_N
0	0	2	2.0	0.7+1.7i	(2.0)f_{Ga}+(0.7+1.7i)f_N
1	0	1	1.5-0.9i	-1.7-0.4i	(1.5-0.9i)f_{Ga}+(-1.7-0.4i)f_N
1	0	2	0.5+0.9i	-0.9+1.3i	(0.5+0.9i)f_{Ga}+(-0.9+1.3i)f_N
1	1	0	0.5-0.9i	1.3-1.0i	(0.5-0.9i)f_{Ga}+(1.3-1.0i)f_N
1	0	3	1.5-0.9i	-0.3-0.5i	(1.5-0.9i)f_{Ga}+(-0.3-0.5i)f_N
2	0	0	0.5-0.9i	1.3-1.0i	(0.5-0.9i)f_{Ga}+(1.3-1.0i)f_N
1	1	2	0.5-0.9i	0.3+0.03i	(0.5-0.9i)f_{Ga}+(0.3+0.03i)f_N
2	0	1	1.5+0.9i	-0.5-1.7i	(1.5+0.9i)f_{Ga}+(-0.5-1.7i)f_N
0	0	4	2.0	-0.3+0.7i	(2.0)f_{Ga}+(-0.3+0.7i)f_N
2	0	2	0.5-0.9i	0.3+0.03i	(0.5-0.9i)f_{Ga}+(0.3+0.03i)f_N
1	0	4	0.5+0.9i	-2.0+0.3i	(0.5+0.9i)f_{Ga}+(-2.0+0.3i)f_N

Table A.2: Results of the wurtzite structure factor calculations.

BIBLIOGRAPHY

[1] P. Dudesek, L. Benco, C. Daul, and K. Schwarz, "d-to-s bonding in GaN," Journal of Physics: Condensed Matter **10,** 7155–7162 (1998).

[2] J. Kolnik, İ. Oğuzman, K. Brennan, R. Wang, P. Ruden, and Y. Wang, "Electronic transport studies of bulk zincblende and wurtzite phases of GaN based on an ensemble Monte Carlo calculation including a full zone band structure," Journal of Applied Physics **78,** 1033 (1995).

[3] A. Maslov and C. Ning, "Band structure and optical absorption of GaN nanowires grown along the c axis," Physical Review B **72,** 125319 (2005).

[4] K. Momma and F. Izumi, "*VESTA*: a three-dimensional visualization system for electronic and structural analysis," Journal of Applied Crystallography **41,** 653–658 (2008).

[5] *Powder Diffraction File 2-1078 Gallium Nitride* (International Centre for Diffraction Data, Swarthmore, Pennsylvania, 1991).

[6] J. A. Jegier, S. McKernan, A. P. Purdy, and W. L. Gladfelter, "Ammonothermal Conversion of Cyclotrigallazane to GaN: Synthesisi of Nanocrystalline and Cubic GaN from $[H_2GaNH_2]_3$," Chemistry of Materials **12,** 1003–1010 (2000).

[7] B. Jacobs, V. Ayres, M. Crimp, and K. McElroy, "Internal structure of multiphase zinc-blende wurtzite gallium nitride nanowires," Nanotechnology **19,** 405706 (2008).

[8] B. Jacobs, M. Crimp, K. McElroy, and V. Ayres, "Nanopipes in Gallium Nitride Nanowires and Rods," Nano Letters **8,** 4353–4358 (2008).

[9] *Preparation and Properties of Solid State Materials: Growth Mechanisms and Silicon Nitride*, W. R. Wilcox, ed., (Marcel Dekker, Inc., 1982), Vol. 7.

[10] F. Phillips, *An Introduction to Crystallography* (Longmans New York, 1963).

[11] T. Hahn and H. Klapper, "3.3. Twinning of crystals," International Tables for Crystallography **D,** 393–448 (2006).

[12] H. Choi, J. Johnson, R. He, S. Lee, F. Kim, P. Pauzauskie, J. Goldberger, R. Saykally, and P. Yang, "Self-Organized GaN Quantum Wire UV Lasers," Journal of Physical Chemistry B **107,** 8721–8725 (2003).

[13] U. Mishra, P. Parikh, and Y. Wu, "AlGaN/GaN HEMTs-An Overview of Device Operation and Applications," Proceedings of the IEEE **90,** 1022–1031 (2002).

[14] C. Thelander *et al.*, "Nanowire-based one-dimensional electronics," Materials Today **9,** 28–35 (2006).

[15] M. Heiß, A. Gustafsson, S. Conesa-Boj, F. Peiró, J. Morante, G. Abstreiter, J. Arbiol, L. Samuelson, and A. Fontcuberta i Morral, "Catalyst-free nanowires with axial InxGa1-xAs/GaAs heterostructures," Nanotechnology **20,** 075603 (2009).

[16] "Gallium Nitride: Band structure and carrier concentaration,", http://www.ioffe.ru/SVA/NSM/Semicond/GaN/bandstr.html.

[17] S. Nakamura, T. Mukai, and M. Senoh, "Candela-class high-brightness InGaN/AlGaN double-heterostructure blue-light-emitting," Applied Physics Letters **64,** 1687–1215 (1994).

[18] T. Fujii, Y. Gao, R. Sharma, E. Hu, S. DenBaars, and S. Nakamura, "Increase in the extraction efficiency of GaN-based light-emitting diodes via surface roughening," Applied physics letters **84,** 855 (2004).

[19] K. Akita, T. Kyono, Y. Yoshizumi, H. Kitabayashi, and K. Katayama, "Improvements of external quantum efficiency of InGaN-based blue light-emitting diodes at high current density using GaN substrates," Journal of Applied Physics **101,** 033104 (2007).

[20] J. Johnson, H. Choi, K. Knutsen, R. Schaller, P. Yang, and R. Saykally, "Single gallium nitride nanowire lasers," Nature Materials **1,** 106–110 (2002).

[21] Y. Huang, X. Duan, and C. Lieber, "Nanowires for Integrated Multicolor Nanophotonics," Small **1,** 142–147 (2005).

[22] M. Khan, J. Kuznia, D. Olson, W. Schaff, J. Burm, and M. Shur, "Microwave performance of a 0.25 μm gate AlGaN/GaN heterostructure field effect transistor," Applied Physics Letters **65,** 1121 (1994).

[23] H. Xing *et al.*, "Gallium nitride based transistors," Journal of Physics: Condensed Matter **13,** 7139–7158 (2001).

[24] S. Pearton, F. Ren, A. Zhang, and K. Lee, "Fabrication and performance of GaN electronic devices," Materials Science & Engineering R **30,** 55–212 (2000).

[25] M. Murphy *et al.*, "High-frequency AlGaN/GaN polarization-induced high electron mobility transistors grown by plasma-assisted molecular-beam epitaxy," Applied Physics Letters **75,** 3653 (1999).

[26] Y. Huang, X. Duan, Y. Cui, and C. Lieber, "Gallium Nitride Nanowire Nanodevices," Nano Letters **1,** 6 (2002).

[27] B. Jacobs, V. Ayres, R. Stallcup, A. Hartman, M. Tupta, A. Baczewski, M. Crimp, J. Halpern, M. He, and H. Shaw, "Electron transport in zinc-blende wurtzite biphasic gallium nitride nanowires and GaNFETs," Nanotechnology **18,** 475710–475710 (2007).

[28] J. Phillips, "The Chemical Bond and Solid-state Physics.," Physics Today **23,** 23–30 (1970).

[29] M. Kanoun, S. Goumri-Said, A. Merad, G. Merad, J. Cibert, and H. Aourag, "Zinc-blende AlN and GaN under pressure: structural, electronic, elastic and piezoelectric properties," Semiconductor Science and Technology **19,** 1220–1231 (2004).

[30] H. Iwanaga, A. Kunishige, and S. Takeuchi, "Anisotropic thermal expansion in wurtzite-type crystals," Journal of Materials Science **35,** 2451–2454 (2000).

[31] T. B. M. Charles S. Barrett, *Structure of Metals: crystallographic methods, principles, and data,* 3rd ed. (McGraw-Hill Book Company, 1966), pp. 614–615.

[32] J. W. Edington, *Practical Electron Microscopy in Materials Science* (TechBooks, 1976), pp. 281–296.

[33] Y. Wu and P. Yang, "Direct Observation of Vapor-Liquid-Solid Nanowire Growth," Journal of the American Chemical Society **123,** 3165–3166 (2001).

[34] W. Seifert *et al.*, "Growth of one-dimensional nanostructures in MOVPE," Journal of Crystal Growth **272,** 211–220 (2004).

[35] Y. Wu, H. Yan, M. Huang, B. Messer, J. Song, and P. Yang, "Inorganic Semiconductor Nanowires: Rational Growth, Assembly, and Novel Properties," Chemistry–A European Journal **8,** 1260–1268 (2002).

[36] C. Chen, C. Yeh, C. Chen, M. Yu, H. Liu, J. Wu, K. Chen, L. Chen, J. Peng, and Y. Chen, "Catalytic growth and characterization of gallium nitride nanowires," Journal of the American Chemical Society **123,** 2791–2798 (2001).

[37] T. Kuykendall *et al.*, "Metalorganic chemical vapor deposition route to GaN nanowires with triangular cross sections," Nano Letters **3,** 1063–1066 (2003).

[38] X. Duan and C. Lieber, "Laser-assisted catalytic growth of single crystal GaN nanowires," Journal of the American Chemical Society **122,** 188–189 (2000).

[39] K. Dick, K. Deppert, T. Mårtensson, B. Mandl, L. Samuelson, and W. Seifert, "Failure of the vapor–liquid–solid mechanism in Au-assisted MOVPE growth of InAs nanowires," Nano Letters **5,** 761–764 (2005).

[40] L. Geelhaar, C. Chèze, W. Weber, R. Averbeck, H. Riechert, T. Kehagias, P. Komninou, G. Dimitrakopulos, and T. Karakostas, "Axial and radial growth of Ni-induced GaN nanowires," Applied Physics Letters **91,** 093113 (2007).

[41] L. Lari, R. Murray, T. Bullough, P. Chalker, M. Gass, C. Chčze, L. Geelhaar, and H. Riechert, "Nanoscale compositional analysis of Ni-based seed crystallites associated with GaN nanowire growth," Physica E: Low-dimensional Systems and Nanostructures **40,** 2475–2461 (2008).

[42] H. Peng, N. Wang, X. Zhou, Y. Zheng, C. Lee, and S. Lee, "Control of growth orientation of GaN nanowires," Chemical Physics Letters **359,** 241–245 (2002).

[43] C. Nam, D. Tham, and J. Fischer, "Effect of the polar surface on GaN nanostructure morphology and growth orientation," Applied Physics Letters **85,** 5676 (2004).

[44] Z. Dai, Z. Pan, and Z. Wang, "Novel Nanostructures of Functional Oxides Synthesized by Thermal Evaporation," Advanced Functional Materials **13,** 9–24 (2003).

[45] A. Sekar, S. Kim, A. Umar, and Y. Hahn, "Catalyst-free synthesis of ZnO nanowires on Si by oxidation of Zn powders," Journal of Crystal Growth **277,** 471–478 (2005).

[46] J. M. Blakely and K. A. Jackson, "Growth of Crystal Whiskers," The Journal of Chemical Physics **37,** 428–430 (1962).

[47] X. Cai, A. Djurišić, M. Xie, C. Chiu, and S. Gwo, "Growth mechanism of stacked-cone and smooth-surface GaN nanowires," Applied Physics Letters **87,** 183103 (2005).

[48] D. Moore and Z. Wang, "Growth of anisotropic one-dimensional ZnS nanostructures," Journal of Materials Chemistry **16,** 3898–3905 (2006).

[49] D. A. Porter and K. E. Easterling, *Phase Transformations in Metals and Alloys* (Chapman & Hall, 1993).

[50] *Handbook of Crystal Growth,* D. T. J. Hurle, ed., (Elsevier, 1993), Vol. 1, pp. 189, 410, 462, 481.

[51] W. K. Burton, N. Cabrera, and F. C. Frank, "The Growth of Crystals and the Equilibrium Structure of their Surfaces," Philosophical Transactions of the Royal Society of London. Series A, Mathematical and Physical Sciences **243,** 299–358 (1951).

[52] P. Bennema, "Spiral Growth and Surface Roughening: Developments Since Burton, Cabrera and Frank," Journal of Crystal Growth **69,** 182 (1984).

[53] *Growth, dissolution, and pattern formation in geosystems*, B. Jamtveit and P. Meakin, eds., (Springer, 1999), p. 23.

[54] J. C. Heyraud and J. J. Metois, "Equilibrium Shape of an Ionic Crystal in Equilibrium with its Vapour (NaCl)," Journal of Crystal Growth **84,** 503–508 (1987).

[55] K. Jackson, "Constitutional supercooling surface roughening," Journal of Crystal Growth **264,** 519–529 (2004).

[56] C. Geng, Y. Jiang, Y. Yao, X. Meng, J. Zapien, C. Lee, Y. Lifshitz, and S. Lee, "Well-aligned ZnO nanowire arrays fabricated on silicon substrates," Advanced Functional Materials **14,** 589–594 (2004).

[57] S. Vaddiraju, A. Mohite, A. Chin, M. Meyyappan, G. Sumanasekera, B. Alphenaar, and M. Sunkara, "Mechanisms of 1D crystal growth in reactive vapor transport: Indium Nitride nanowires," Nano Letters **5,** 1625 (2005).

[58] M. He, P. Zhou, S. Mohammad, G. Harris, J. Halpern, R. Jacobs, W. Sarney, and L. Salamanca-Riba, "Growth of GaN nanowires by direct reaction of Ga with NH3," Journal of Crystal Growth **231,** 357–365 (2001).

[59] A. ElAhl *et al.*, "Systematic study of effects of growth conditions on the (nano-, meso-, micro) size and (one-, two-, three-dimensional) shape of GaN single crystals grown by a direct reaction of Ga with ammonia," Journal of Applied Physics **94,** 7749 (2003).

[60] D. Williams and C. Carter, *Transmission Electron Microscopy: A Textbook for Materials Science* (Springer, 1996), pp. 186–187, 463.

[61] V. Ayres *et al.*, "Investigations of heavy ion irradiation of gallium nitride nanowires and nanocircuits," Diamond & Related Materials **15,** 1117–1121 (2006).

[62] B. Jacobs, V. Ayres, M. Petkov, J. Halpern, M. He, A. Baczewski, K. McElroy, M. Crimp, J. Zhang, and H. Shaw, "Electronic and Structural Characteristics of Zinc-Blende Wurtzite Biphasic Homostructure GaN Nanowires," Nano Letters **7,** 1435–1438 (2007).

[63] V. Ayres, M. Farhan, D. Spach, J. Bobbitt, J. Majeed, B. Wright, B. Wright, J. Asmussen, M. Kanatzidis, and T. Bieler, "Transitions in morphology observed in nitrogen/methane–hydrogen depositions of polycrystalline diamond films," Journal of Applied Physics **89,** 6062 (2001).

[64] *Chapter 7: Basics of X-ray Diffraction*, Scintag, Inc., Cupertino, CA, 1999.

[65] M. Buerger, "The genesis of twin crystals," American Mineralogist **30,** 469–482 (1945).

[66] *International Tables for Crystallography*, T. Hahn, ed., (Springer - Verlag, 2005), Vol. C, pp. 553–564.

[67] "Wolfram MathWorld: Triangular Pyramid,", http://mathworld.wolfram.com/TriangularPyramid.html.

[68] "Gallium Nitride: Basic Parameters for Wurtzite crystal structure,", http://www.ioffe.rssi.ru/SVA/NSM/Semicond/GaN/basic.html.